Observational constraints on the evolution of dust in protoplanetary disks

Martins e Oliveira, I.

6

On the Evolution of Dust Mineralogy: from Protoplanetary Disks to Planetary Systems

Mineralogical studies of silicate features emitted by dust grains in protoplanetary disks and Solar System bodies can shed light on the progress of planet formation. The significant fraction of crystalline material in comets, chondritic meteorites and interplanetary dust particles indicates a modification of the almost completely amorphous interstellar medium (ISM) dust from which they formed. The production of crystalline silicates, thus, must happen in protoplanetary disks, where dust evolves to build planets and planetesimals. Different scenarios have been proposed, but it is still unclear how and when this happens. This paper presents dust grain mineralogy (composition, crystallinity and grain size distribution) of a complete sample of protoplanetary disks in the young Serpens cluster. These results are compared to those in the young Taurus region and to sources that have retained their protoplanetary disks in the older Upper Scorpius and η Chamaeleontis stellar clusters, using the same analysis technique for all samples. This comparison allows an investigation of the grain mineralogy evolution with time for a total sample of 139 disks. The mean cluster age and disk fraction are used as indicators of the evolutionary stage of the different populations. Our results show that the disks in the different regions have similar distributions of mean grain sizes and crystallinity fractions ($\sim$10 – 20%) despite the spread in mean ages. Furthermore, there is no evidence of preferential grain sizes for any given disk geometry, nor for the mean cluster crystallinity fraction to increase with mean age in the 1 – 8 Myr range. The main implication is that a modest level of crystallinity is established in the disk surface early on ($\leq$ 1 Myr), reaching an equilibrium that is independent of what may be happening in the disk midplane. These results are discussed in the context of planet formation, in comparison with mineralogical results from small bodies in our own Solar System.

Isa Oliveira, Johan Olofsson, Klaus M. Pontoppidan, Ewine F. van Dishoeck,
Jean-Charles Augereau & Bruno Merín

6.1   Introduction

Protoplanetary disks originate from dense cloud material consisting of sub-μm sized, almost completely amorphous interstellar medium (ISM) dust grains (Beckwith et al. 2000; Li & Draine 2001; Kemper et al. 2004; Henning 2010). The dust and gas in these disks form the basic matter from which planets may form. At the same time, mineralogical studies of primitive solar system bodies suggest that a considerable fraction of the silicate grains in these objects are of crystalline nature (Wooden et al. 2007; Pontoppidan & Brearley 2010, and references therein). It is then naturally implied that the crystallinity fraction increases, through thermal and chemical modification of these solids during the general planet formation process, commonly referred to in the literature as "disk evolution".

As time passes, the small dust responsible for the infrared (IR) excess observed around young stars is subjected to different processes that affect, and will eventually determine how this progression will end. Planets and planetary systems have been observed around hundreds of stars other than the Sun, showing that this result is rather common (Udry & Santos 2007). IR observations have revealed a great number of *debris disks*, composed of large planetesimal rocks and smaller bodies, around a variety of stars spanning a large range in spectral types and ages (Rieke et al. 2005; Bryden et al. 2006; Su et al. 2006; Gautier et al. 2007; Carpenter et al. 2009). A few debris disks are known to harbor planets (e.g., β Pictoris and Fomalhaut, Lagrange et al. 2010; Kalas et al. 2008), although it is still unclear whether this is often true (Kóspál et al. 2009). The majority of main-sequence stars show no signs of planets or debris within the current observational limitations, however, indicating that the disks around such stars at the time of their formation have dissipated completely, leaving no dust behind to tell the story. Which processes are important and determinant for the aftermath of disk evolution are still under debate, and this topic is the subject of many theoretical and observational studies over the last decade, stimulated in large by recent IR and (sub-)millimeter facilities.

Specifically on the subject of the mineralogical composition, spectra from the ground and the *Infrared Space Observatory* gave the first clues of a potential link between crystalline material in protoplanetary disks and comets. A great similarity was noted between the spectra of the disk around the Herbig star HD 100546 and that of comet Hale-Bopp (Crovisier et al. 1997; Malfait et al. 1998). More recently, the InfraRed Spectrograph (IRS, $5-38$ μm, Houck et al. 2004) on-board the *Spitzer Space Telescope* allowed an unprecedented combination of high sensitivity and the ability to observe large numbers of disks, down to the brown dwarf limit. The shape of the silicate features probed by the IRS spectra at 10 and 20 μm is affected by the composition, size and structure of its emitting dust. Amorphous silicates show broad smooth mid-IR features, while the opacities of crystalline grains show sharp features due to their large-scale lattice arrangement, such that even small fractions of crystalline grains produce additional structure in the silicate features (Min et al. 2005; Bouwman et al. 2008; Juhász et al. 2009; Olofsson et al. 2010). Because most

protoplanetary disks are optically thick at optical and IR wavelengths, the silicate features observed in the mid-IR are generally emitted by dust in the optically thin disk surface only. To probe the disk midplane, observations at longer wavelengths are necessary. Additionally, the emission at 10 and 20 μm has been shown to arise from different grain populations, probing different radii (Kessler-Silacci et al. 2006; Olofsson et al. 2009, 2010). While the 10 μm feature probes a warmer dust population, at $\leq$ 1 AU for T Tauri stars, the dust emitting at 20 μm is colder, further out and deeper into the disk (Kessler-Silacci et al. 2007).

Two methods have been proposed to explain the formation of crystal grains: thermal annealing of amorphous grains or vaporization followed by gas-phase condensation. Both methods require high temperatures (above $\sim$1000 K, Fabian et al. 2000; Gail 2004) which is inconsistent with outer disk temperatures. However, crystalline grains have been observed in outer, as well as in inner disks (van Boekel et al. 2004). Large-scale radial mixing has been invoked to explain the presence of crystals at low temperatures in the outer disk (Bockelée-Morvan et al. 2000; Gail 2004; Ciesla 2009). A third proposed formation mechanism for crystal formation is that shock waves could locally heat amorphous silicates and crystallize them (Desch & Connolly 2002; Harker & Desch 2002).

From protoplanetary disks to comets, several authors have attempted to infer the dust composition from IRS spectra and laboratory data on amorphous and crystalline silicate dust, using a variety of analysis techniques. Whether for individual objects (Forrest et al. 2004; Merín et al. 2007; Pinte et al. 2008; Bouy et al. 2008), for mixed disk samples (Bouwman et al. 2001; Apai et al. 2005; van Boekel et al. 2005; Bouwman et al. 2008; Olofsson et al. 2009, 2010; Juhász et al. 2010), or systematic studies of the disk population of a given star-forming region (Sicilia-Aguilar et al. 2009; Watson et al. 2009; Sargent et al. 2009), it has been shown that a significant mass fraction of the dust in those disks must be in crystalline form. However, the many studies dealing with the mineralogical composition of dust to date focus on a specific region or object, failing to investigate the hypothesis that the crystallinity fraction is a measure of the evolutionary stage of a region. That is, no study in the literature has yet investigated an increase of crystallinity fraction with cluster age.

Mineralogical studies of Solar System bodies show a range of crystallinity fractions. Evidence from primitive chondrites shows that the abundance of crystalline silicate material varies from nearly nothing up to 20 – 30 % (e.g. Acfer 094 and ALH77307, Pontoppidan & Brearley 2010 and references therein). Oort cloud comets, with long periods and large distances from the Sun, have inferred crystallinity fractions up to 60 – 80 % (e.g. Hale-Bopp, Wooden et al. 1999, 2007). Jupiter-family, or short period comets, have lower fractions, up to $\sim$35 % (e.g. 9P/Tempel 1, Harvey et al. 2007b; 81P/Wild 2, Zolensky et al. 2006). This discrepancy in fractions points to the existence of a radial dependence in crystallinity fraction in the protoplanetary disk around the young Sun (Harker et al. 2005). It is important to note that those values are model dependent, and the use of large amorphous grains (10 – 100 μm) can lead to systematically lower crystalline fractions (Harker et al. 2002). This is evident for

Hale-Bopp, where Min et al. (2005) find a much lower fraction ($\sim$7.5 %) than other authors, using a distribution of amorphous grain sizes up to 100 μm. What is clear is that even within the discrepancies, the crystallinity fractions derived for Solar System bodies are appreciably higher than those derived for the ISM dust ($< 2\%$, Kemper et al. 2004). Recent *Spitzer* data indicate further similarities between crystalline silicate features seen in comets or asteroids with those seen in some debris disks around solar mass stars (Beichman et al. 2006; Lisse et al. 2007, 2008). One proposed explanation is that the observed spectral features in the disk result from the catastrophic break-up of a single large body (a 'super comet') which creates the small dust particles needed for detection. At the even earlier protoplanetary disk stage, there is limited observational evidence for radial gradients in crystallinity from mid-infrared interferometry data, with higher crystallinity fractions found closer to the young stars (van Boekel et al. 2004; Schegerer et al. 2008). All of this suggests that the crystallization occurs early in the disk evolution and is then incorporated into larger solid bodies.

Besides dust composition, the evolution of grain sizes is an essential indicator of disk evolution. The initially sub-μm size ISM grains must grow astounding 14–15 orders of magnitude in diameter if they are to form planets. If grains were to grow orderly and steadily, theoretical calculations predict disks to have fully dissipated their small grains within $\sim$10^5 years (Weidenschilling 1980; Dullemond & Dominik 2005). The fact that many disks a few Myr old are observed to have small grains (Hernández et al. 2008) poses a serious problem for the paradigm that grain growth is a steady, monotonic process in disk evolution and planet formation. Additionally, small dust has been observed in the surface layers of disks in clusters of different ages and environments for hundreds of systems. The implications, as discussed most recently by Oliveira et al. (2010) and Olofsson et al. (2010), is that small grains must be replenished by fragmentation of bigger grains, and that an equilibrium between grain growth and fragmentation is established. Oliveira et al. (2010) have shown that this equilibrium is maintained over a few million years, as long as the disks are optically thick, and is independent of the population or environment studied.

In this paper we present a comprehensive study of the mineralogical composition of disks around stars in young star-forming regions (where most stars are still surrounded by optically thick disks) and older clusters (where the majority of disks has already dissipated). Correlating the results on mean size and composition of dust grains per region, obtained in a homogeneous way using the same methodology, with the properties of small bodies in our own Solar System can put constraints on some of the processes responsible for disk evolution and planet formation. The Serpens Molecular Cloud, whose complete flux-limited YSO population has been observed by the IRS instrument (Oliveira et al. 2010), is used as a prototype of a young star-forming region, together with Taurus, the best studied region to date. The sources that have retained their protoplanetary disks in the η Chamaeleontis and Upper Scorpius clusters are used to probe the mineralogy in the older bin of disk evolution.

Section 6.2 describes the YSO samples in the 4 regions mentioned. The *Spitzer* IRS observations and reduction are explained. The spectral decomposition method B2C

(Olofsson et al. 2010) is briefly introduced in § 6.3, and its results for individual and mean cluster grain sizes and composition are shown in § 6.4. In § 6.5 the results are discussed in the context of time evolution. There we demonstrate that no evolution is seen in either mean grain sizes or crystallinity fractions as clusters evolve from ∼1 to 8 Myr. The implications for disk formation and dissipation, and planet formation are discussed. In § 6.6 we present our conclusions.

6.2   Spitzer IRS Data

The four regions presented here were chosen due to the availability of complete sets of IRS spectra of their IR-excess sources, while spanning a wide range of stellar characteristics, environment, mean ages and disk fractions (the disk fraction of Serpens is still unknown, see Table 6.1).

The IRS spectra of a complete flux-limited sample of young stellar objects (YSO) in the Serpens Molecular Cloud have been presented by Oliveira et al. (2010), based on program ID #30223 (PI: Pontoppidan). As detailed there, the spectra were extracted from the basic calibration data (BCD) using the reduction pipeline from the Spitzer Legacy Program "From Molecular Cores to Planet-Forming Disks" (c2d, Lahuis et al. 2006). A similarly large YSO sample in the Taurus star-forming region has been presented by Furlan et al. (2006). IRS spectra of all 18 members of the η Chamaeleontis cluster were first shown by Sicilia-Aguilar et al. (2009), while the spectra of 26 out of the 35 IR-excess sources in the Upper Scorpius OB association were shown by Dahm & Carpenter (2009) (the remaining 9 objects were not known at the time the observations were proposed). For the latter 3 regions, the post-BCD data were downloaded from the SSC pipeline (version S18.4) and then extracted with the Spitzer IRS Custom Extraction software (SPICE, version 2.3) using the batch generic template for point sources. As a test, the IRS spectra of the YSOs in Serpens were also reduced using SPICE to ensure that both pipelines produce nearly identical results. On visual inspection, no discrepancies were found between the results from the two pipelines, all objects showed the exact same features in both spectra. The similarity in outputs is such that the effects on the spectral decomposition results are within the cited error bars.

Since the spectral decomposition method applied here aims to reproduce the silicate emission from dust particles in circumstellar disks, the sample has been limited to spectra that show clear silicate features. The few sources with PAH emission have been excluded from the sample. PAH sources amount to less than 8% in low-mass star-forming regions (Geers et al. 2006; Oliveira et al. 2010). Furthermore, spectra with very low signal-to-noise ratios (S/N) are excluded from the analysed sample in order to guarantee the quality of the results. In addition, for objects #114 and 137 in Serpens, and 04370+2559 and V955 Tau in Taurus the warm component fit contributes to most of the spectrum, leaving very low fluxes to be fitted by the cold component. This produces large uncertainties in the cold component fit, and they are therefore not further used in the analysis. The low S/N objects rejected amount to less than

10 % of each of the Serpens and Taurus samples, so the statistical results derived here should not be affected by this removal. The final sample of 139 sources analysed is composed of 60 objects in Serpens, 66 in Taurus, 9 objects in Upper Scorpius, and 4 in η Chamaeleontis. The statistical uncertainties of the spectra were estimated as explained in Olofsson et al. (2009).

The great majority of the objects studied here are low-mass stars (spectral types K and M, see Tables A.1 and A.2). The study of mineralogical evolution across stellar mass is not the focus of this paper. Such a study would require a separate paper, in which the same techniques are used for low- and intermediate-mass stars. Thus, the statistical results derived in the following sections concern T Tauri stars, and not necessarily apply to intermediate-mass Herbig Ae/Be stars.

6.3   Spectral Decomposition and the B2C Method

In order to reproduce the observed IRS spectra of these circumstellar disks the B2C decomposition method, explained in detail and tested extensively in Olofsson et al. (2010), is applied. Two dust grain populations, or components, at different temperatures (warm and cold) are used in the method, in addition to a continuum emission. The warm component reproduces the 10 μm feature, while the cold component reproduces the non-negligible residuals at longer wavelengths, over the full spectral range (see Figure 6.1). Each component, warm and cold, is the combination of five different dust species and three grain sizes for amorphous silicates or two grain sizes for crystalline silicates.
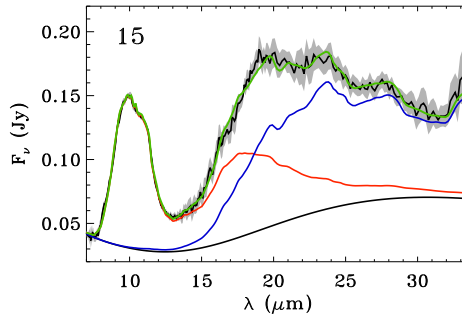
Figure 6.1 – Example of the B2C modeling for object #15 in Serpens. The down-most black line is the estimated continuum for this source. The dark gray line is the fit to the warm component (fitting well the 10 μm feature) and the black line is the fit to the cold component (contributing mostly to longer wavelengths). The light gray line is the final fit to the entire spectrum. The original spectrum is shown in black with its uncertainties in light grey. (A color version of this figure is available in the online journal)

The three amorphous species are silicates of olivine stoichiometry ($MgFeSiO_4$), silicates of pyroxene stoichiometry ($MgFeSiO_6$), and silica (SiO_2). The two crystalline species are both Mg-rich end members of the pyroxene and olivine groups, enstatite

(MgSiO$_3$) and forsterite (Mg$_2$SiO$_4$). As further explained in Olofsson et al. (2010), the theoretical opacities of the amorphous species are computed assuming homogeneous spheres (Mie theory), while those for the crystalline species use the distribution of hollow spheres (DHS, Min et al. 2005) theory so that irregularly shaped particles can be simulated.

In addition, the three grain sizes used are 0.1, 1.5 and 6.0 μm, representing well the spectroscopic behaviour of very small, intermediate-sized and large grains. For the crystalline species, however, the code is limited to only 2 grain sizes (0.1 and 1.5 μm). This restriction is imposed because large crystalline grains are highly degenerate with large amorphous grains (as can be seen in Figure 1 of Olofsson et al. 2010), and because the production of large 6.0 μm pure crystals is not expected via thermal annealing (Gail 2004).

The B2C method itself consists of three steps. First, the continuum is estimated and subtracted from the observed spectrum. The adopted continuum is built by using a power-law plus a black-body at temperature T_{cont}. The power-law represents the mid-IR tail of emission from the star and inner disk rim. The black-body is designed to contribute at longer wavelengths, and is therefore constrained to be less than 150 K. Each dust component is then fitted separately to the continuum-subtracted spectrum.

The second step is to fit the warm component to reproduce the 10 μm silicate feature between $\sim$7.5 and 13.5 μm. This is done by summing up the 13 mass absorption coefficients ($N_{\text{species}} = 5$, $N_{\text{sizes}} = 3$ or 2, for amorphous and crystalline species, respectively), multiplied by a black-body $B_\nu(T_{\text{w}})$ at a given warm temperature T_{w}.

The third step is to fit the residuals, mostly at longer wavelengths, over the entire spectral range (5 – 35 μm). This is done in a similar manner, for a given cold temperature T_{c}. The final fit is a sum of the three fits described, as can be seen in Figure 6.1. The entire fitting process is based on a Bayesian analysis, combined with a Monte Carlo Markov chain, in order to randomly explore the space of free parameters. The resulting mean mass-average grain size is the sum of all sizes fitted, each size being weighted by their corresponding masses, as:

$$\langle a_{\text{warm/cold}} \rangle = \left(\sum_{j=1}^{N_{\text{sizes}}} a_j \sum_{i=1}^{N_{\text{species}}} M_{\text{w/c},i}^j \right) \times \left(\sum_{j=1}^{N_{\text{sizes}}} \sum_{i=1}^{N_{\text{species}}} M_{\text{w/c},i}^j \right)^{-1} \tag{6.1}$$

where $a_1 = 0.1 \, \mu$m (small grains), $a_2 = 1.5 \, \mu$m (intermediate-sized grains) and $a_3 = 6 \, \mu$m (large grains). Further details and tests of the B2C procedure can be found in Olofsson et al. (2010). That paper also demonstrates that the procedure is robust for statistical samples, and that the relative comparisons between samples, which are the focus of this paper, should not suffer from the assumptions that enter in the procedure. The robustness of the procedure is evaluated by fitting synthetic spectra, and is discussed in detail in their Appendix A. The influence of the continuum estimate is also discussed, especially for the cold component for both grain sizes and crystallinity fractions, and it is shown that prescriptions that do not use large 6 μm grains (which are, to some degree, degenerate with the continuum) give fits that are not so good.

For the amorphous grains, the B2C procedure uses the Mie scattering theory to compute mass absorption coefficients. However, Min et al. (2007) found that they could best reproduce the extinction profile toward the galactic center using the DHS scattering theory, with a maximum filling factor of 0.7. The most striking difference between Mie and DHS mass absorption coefficients is seen for the O–Si–O bending mode around 20 μm. Here we investigate the influence of the use of DHS instead of Mie for amorphous grain with an olivine or pyroxene stoichiometry. We conducted tests on a sub-sample of 30 objects (15 in Serpens and 15 in Taurus). The conclusion of such tests is that it has a small influence on the quantities we discuss in this study. For the warm component of the 30 objects, we find a change in the mean crystallinity fraction of -1.6% (the mean crystallinity for this sub-sample using DHS is 9.3% versus 10.9% using Mie), which is in the range of uncertainties claimed in this study. We also computed the mean slope of grain size distributions to gauge the effect of using DHS on grain sizes. On average, the grain size distribution indices are steeper by $\sim$0.2 (with a mean slope of -3.01 for this sub-sample using DHS versus -2.80 using Mie). Therefore, our main conclusions are preserved for the warm component. Concerning the cold component, the inferred crystallinity fraction using DHS is 22.5% versus 15.1% with Mie, a mean increase of 7.4%. For the mean slope of grain size distributions, a negligible decrease is found (-3.07 using DHS versus -3.01 for Mie). Again, the differences found are within our significant errors for the cold component and do not change any of our conclusions.

It is important to note that the S/N generally degrades at longer wavelengths when compared to shorter wavelengths. The lower S/N reflect on the cold component fits and will most likely result in larger uncertainties. We evaluate that the fits to the cold component are reliable and add important information on the dust mineralogy (albeit with larger uncertainties) and thus those results are included in the following discussion.

6.4   Results

The IRS spectra of the 139 YSOs with IR excess discussed in § 6.2 were fitted with the B2C spectral decomposition procedure. The relative abundances derived for all objects are shown in Appendix A. The S/N drops considerably for the long wavelength module of some of the objects studied (including all objects in Upper Scorpius and η Chamaeleontis). For this reason, the cold component could not be satisfactorily fitted and no results for this component are presented for these sources (see Appendix A).

Due to the large number of objects, these results allow statistical studies on both the mineralogy and size distribution of the grains that compose the optically thin surface layers of disks in each cluster studied. The mean abundances of each species per region are presented in Table 6.2, where it can be seen that the majority of the dust studied is of amorphous form. In Table 6.3 the mean mass-average grain sizes and crystallinity fractions per region are shown. Mean sizes are in the range $1 - 3$ μm, without significant difference between regions. These results are discussed in detail

in the following sections.

It is important to note that the comparison of results derived here for the different regions is valid because the same method, with exact same species, is used for all sources. The comparison of samples analyzed in distinct ways can lead to differences in results that do not correspond to real differences in composition. Nevertheless, in § 6.4.5 the results presented here are compared to literature results for the same objects, when available, with generally good agreement.

6.4.1   Grain Sizes

The mean mass-averaged grain sizes for the warm ($\langle a_{\mathrm{warm}} \rangle$) and cold ($\langle a_{\mathrm{cold}} \rangle$) components are shown in Figure 6.2, for Serpens and Taurus (for the objects in Upper Sco and η Cha no results for the cold component are not available, see Appendix A). It is seen that the two clouds overlap greatly, and that the grain sizes derived from the different temperature components do not seem to correlate. To quantify this correlation, a Kendall τ correlation coefficient can be computed together with its associated probability P (between 0 and 1). $\tau = 1(-1)$ defines a perfect correlation (anti-correlation), and $\tau = 0$ means that the datasets are completely independent. A small P, on the other hand, testifies to how tight the correlation is. For the warm and cold mean mass-averaged grain sizes for both clouds, τ is found to be 0.14, with $P = 0.07$. This lack of correlation indicates that different processes are likely responsible for regulating the size distribution at different radii (Olofsson et al. 2010).
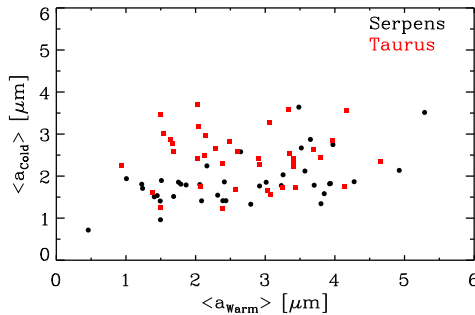
Figure 6.2 – Mass-averaged mean grain sizes for the warm ($\langle a_{\mathrm{warm}} \rangle$) and cold ($\langle a_{\mathrm{cold}} \rangle$) components. Black dots are the objects in Serpens, and gray squares are the objects in Taurus. (A color version of this figure is available in the online journal)

Although the average grain size in the warm component is bigger than that in the cold component within a given star-forming region, as shown in Table 6.3, this difference is mostly not significant. However, Figures 6.2 and 6.3 clearly show a difference between the range of grain sizes spanned in both components, with $\langle a_{\mathrm{cold}} \rangle$ never reaching near the biggest grain size modeled (6.0 μm) for any object. A possible explanation for larger grains at smaller radii, suggested by Sargent et al. (2009), is

that grains coagulate faster in the inner disk where dynamical timescales are shorter. However as discussed by Oliveira et al. (2010) and in § 6.5.1, the mean dust size at the disk surface is not regulated by grain growth alone, but also by fragmentation and vertical mix. This means that faster coagulation at smaller radii cannot be uniquely responsible for bigger grains in the inner disk. Future modeling should try to understand this difference in mean grain sizes observed.
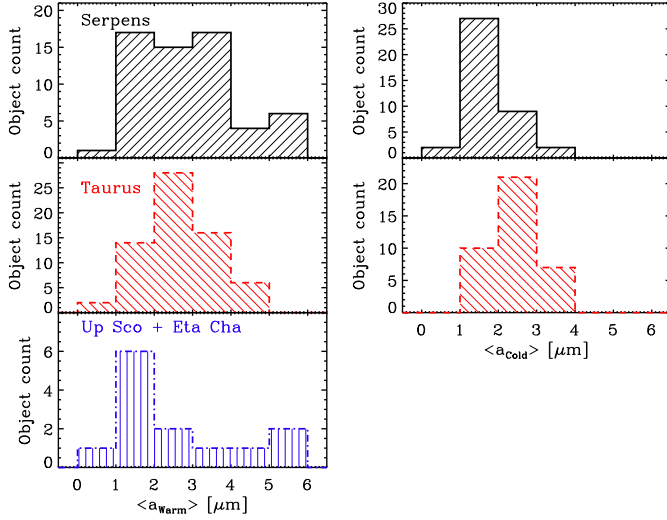
Figure 6.3 – Distribution of mass-averaged mean grain sizes for the warm ($\langle a_{\mathrm{warm}} \rangle$, left panel) and cold ($\langle a_{\mathrm{cold}} \rangle$, right panel) components. Due to the low number statistics, the objects in Upper Sco and η Cha have been merged together as an older cluster. (A color version of this figure is available in the online journal)

Furthermore, Serpens and Taurus occupy an indistinguishable locus in Figure 6.2, explicitly seen in Figure 6.3. A two sample Kolmogorov-Smirnov test (KS-test) was performed and the results show that the null hypothesis that the two distributions come from the same parent population cannot be rejected to any significance (14%). The older regions, although lacking statistical significance, show a distribution of mass-average grain sizes in the same range probed by the young star-forming regions (Figure 6.3). This supports the evidence that the size distribution of the dust in the surface layers of disks is statistically the same independent of the population studied (Oliveira et al. 2010).

The results here confirm those from Olofsson et al. (2010) that the mean differential grain size distributions slope for the three grain sizes considered are shallower than the reference MRN differential size distribution ($\alpha = -3.5$). The mean grain size distributions slopes (α) for each region can be found in Table 6.3.

6.4.2   Disk Geometry

The amount of IR-excess in a disk is directly related to its geometry (Kenyon & Hartmann 1987; Meeus et al. 2001; Dullemond et al. 2001). Specifically using the IRS spectra, disk geometry can be inferred from the flux ratio between 30 and 13 μm (F_{30}/F_{13}, Brown et al. 2007; Oliveira et al. 2010; Merín et al. 2010). A flared geometry ($1.5 \lesssim F_{30}/F_{13} \lesssim 5$), with considerable IR excess and small dust, allows the uppermost dust layers to intercept stellar light at both the inner and outer disk. For flat disks ($F_{30}/F_{13} \lesssim 1.5$) with little IR excess, only the inner disk can easily intercept the stellar radiation as the outer disk is shadowed. Moreover, cold or transitional disks are interesting objects that present inner dust gaps or holes, producing a region with little or no near-IR excess ($5 \lesssim F_{30}/F_{13} \lesssim 15$). It is interesting to explore the effect of disk geometry on both the mean mass-average grain sizes and crystallinity fractions of the disks studied.
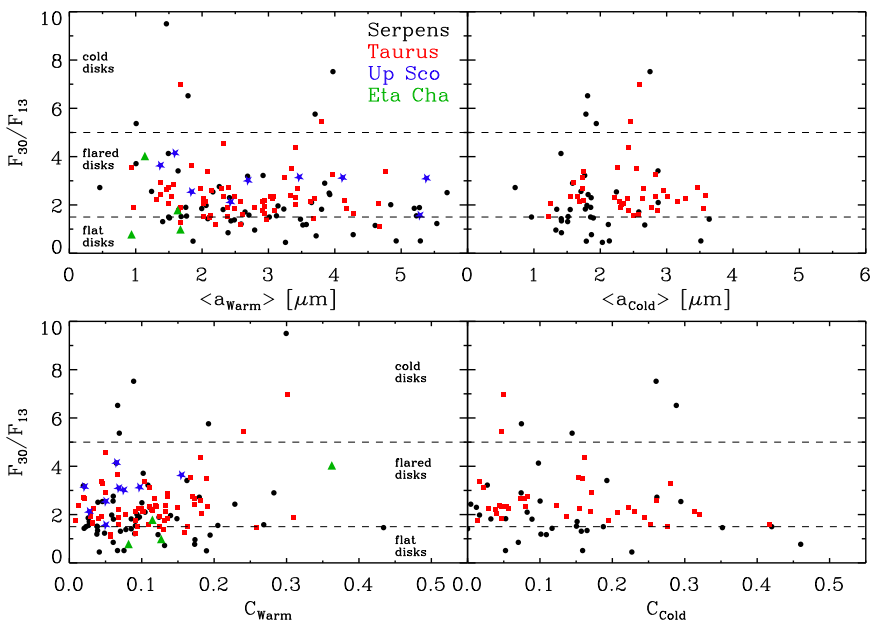
Figure 6.4 – Top: Flaring index F_{30}/F_{13}, used as a proxy for disk geometry, versus warm (left) and cold (right) mass-averaged mean grain sizes. Bottom: F_{30}/F_{13} versus warm (left) and cold (right) crystallinity fractions. The YSOs in Serpens (black dots), Taurus (gray squares), Upper Sco (gray stars), and η Cha (gray triangles) are compared. (A color version of this figure is available in the online journal)

Figure 6.4 shows F_{30}/F_{13} as a proxy for disk geometry compared with the mean mass-averaged grain sizes and crystallinity fractions for both components and all regions studied here. No preferential grain size (correlation coefficient $\tau = -0.14$, $P = 0.02$, and $\tau = 0.07$, $P = 0.33$ for warm and cold components, respectively) nor
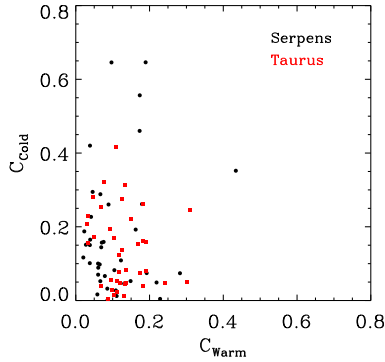
Figure 6.5 – Crystalline fraction of the warm and cold components in Serpens (black dots) and Taurus (gray squares). (A color version of this figure is available in the online journal)

crystallinity fraction ($\tau = 0.09$, $P = 0.10$ for the warm, and $\tau = -0.19$, $P = 0.01$ for the cold component) is apparent for any given disk geometry. Similar scatter plots result for the mean mass-average grains sizes for only amorphous ($\tau = -0.12$, $P = 0.08$ for the warm, and $\tau = 0.13$, $P = 0.11$ for the cold component), or only crystalline grains ($\tau = 0.08$, $P = 0.17$ for the warm, and $\tau = -0.13$, $P = 0.10$ for the cold component). Furthermore, no clear separation is seen between the different regions studied. The statistically relevant samples in Serpens and Taurus define a locus where the majority of the objects is located in each plot, which is followed by the lower number statistics for older regions. Figure 6.4 therefore shows not only that grain size and crystallinity fraction are not a function of disk geometry, but also that younger and older regions show similar distributions of those two parameters.

6.4.3 Crystallinity Fraction

The crystallinity fractions derived from the warm and cold components (C_{Warm} and C_{Cold}, respectively) for Serpens and Taurus are show in Figure 6.5. No strong trend of warm and cold crystallinity fractions increasing together is seen ($\tau = 0.10$, with $P = 0.10$ for the entire sample). This fact implies that, if an unique process is responsible for the crystallization of dust at all radii, this process is not occurring at the same rate in the innermost regions as further out in the disk. This is opposite to the conclusion of Watson et al. (2009), who derive a correlation between inner and outer disk crystallinity from the simultaneous presence of the 11.3 and 33 μm features. The opacities of the crystalline species are more complex than those two features alone, making the analysis here more complete than that of Watson et al. (2009). Our finding that the fraction of crystalline material in disk surfaces varies with radius can constrain some of the mechanisms for formation and distribution of crystals.

A wider spread in crystallinity fraction is observed for the cold component than
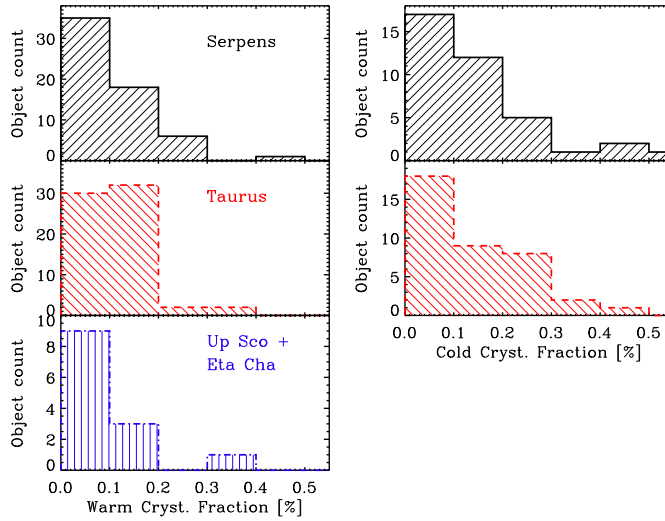
Figure 6.6 − Distribution of crystalline fractions for Serpens (top), Taurus (middle), and Upper Sco and η Cha combined (bottom). Similar distributions and the same range of fractions are seen for all clusters. (A color version of this figure is available in the online journal)

for the warm component (Figure 6.6), which is reflected in the mean crystallinity fractions for each sample (Table 6.3). This discrepancy could be real, or an artifact due to the signal-to-noise ratio (S/N) being frequently lower at longer wavelengths (cold component) than that at shorter wavelengths (warm component), introducing a larger scatter. The difference in Serpens is more significant ($\langle C_{\text{warm}} \rangle \simeq 11.0\%$ and $\langle C_{\text{cold}} \rangle \simeq 17.5\%$). The left panel of Figure 6.7 shows the cumulative fractions as functions of crystallinity fractions. Despite small differences between the warm (red line) and cold (blue line) components, the two cumulative fractions have similar behavior. If this difference is true, there is a small fraction of T Tauri disks with a higher cold (outer) than warm (inner) crystallinity fraction. This finding contrasts with that derived by van Boekel et al. (2004) for the disks around 3 Herbig stars. Their spatially resolved observations infer higher crystallinity fractions in the inner than in the outer disks, albeit based on only 10 μm data. A larger sample of objects with good S/N including both 10 and 20 μm data is needed to better constrain this point. In addition, Figure 6.6 shows that younger and older clusters have similar distributions of crystallinity fractions.

As discussed by many authors, both the grain size and the degree of crystallinity affect the silicate features, therefore it is interesting to search for trends between these two parameters. In Figure 6.8, the mass-average grain sizes are compared to the crystallinity fraction for both warm (left panel) and cold (right panel) components. No obvious trends are seen in either component, neither any separation between regions. This result supports the discussion of Olofsson et al. (2010) that whatever processes
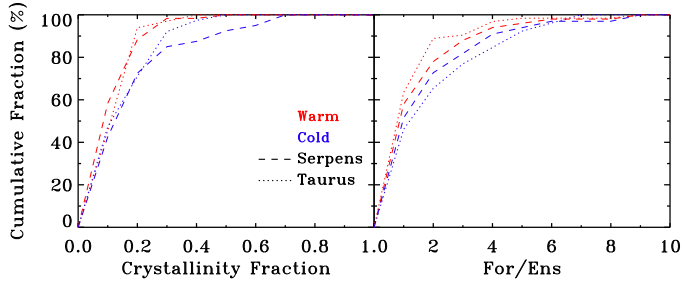
Figure 6.7 – Left: Cumulative fractions of the crystallinity fractions, for Serpens (dashed line) and Taurus (dotted line). Right: Cumulative fraction of the ration between the forsterite and enstatite fractions, for Serpens (dashed line) and Taurus (dotted line). The warm component is shown in light gray while the cold component is dark gray. (A color version of this figure is available in the online journal)

govern the mean grain size and the crystallinity in disks, they are independent from each other.
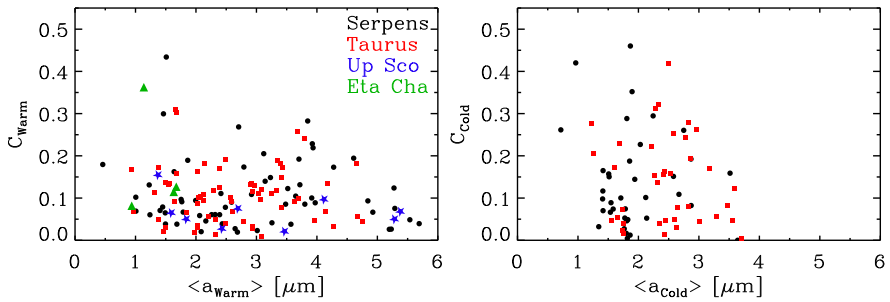
Figure 6.8 – Mass-averaged mean grain sizes versus the crystalline fraction for Serpens (black dots), Taurus (gray squares), Upper Sco (gray stars), and η Cha (gray triangles). (A color version of this figure is available in the online journal)

6.4.3.1 Enstatite vs. Forsterite

The disk models of Gail (2004) consider chemical equilibrium of a mixture of solid and gas at high temperatures, allowing radial mixing of material. These models predict a predominance of forsterite in the innermost regions of the disk, while enstatite dominates at lower temperatures (being converted from forsterite). From the observational point of view, data on disks around T Tauri (Bouwman et al. 2008) and Herbig Ae/Be stars (Juhász et al. 2010) have shown the opposite trend: enstatite is more concentrated in the inner disk, while forsterite dominates the colder, outer disk region. Bouwman et al. (2008) interpret this result as a radial dependence of the species formation mechanisms, or a non-equilibrium of the conditions under which

the species formed, contrary to the models assumptions.

For the regions presented in this study, it can be seen in Table 6.2 for mean cluster values and in Tables A.1 and A.2 for individual objects that the results derived from this study generally follow those of Bouwman et al. (2008), with more enstatite in the warm component and, to a lesser extent, more forsterite in the cold component. The right panel of Figure 6.7 illustrates this for the cumulative fraction of the forsterite over enstatite ratios for individuals disks. However, this trend is not very significant given the uncertainties.

6.4.4   The Silicate Strength-Shape Relation

A correlation between the shape and the strength of the 10 μm silicate feature from disks has been discussed extensively in the literature (van Boekel et al. 2003; Kessler-Silacci et al. 2006; Olofsson et al. 2009; Pascucci et al. 2009; Oliveira et al. 2010; Olofsson et al. 2010). Synthetic 10 μm features generated for different grain sizes and compositions have been shown to fit well with observations, yielding grain size as the important parameter responsible for such a relationship. The degree of crystallinity of the dust also plays a role on the shape of this feature. However, as clearly shown for EX Lup (Ábrahám et al. 2009), and supported by models (Min et al. 2008; Olofsson et al. 2009), an increase in crystallinity fraction does not change the strength of the feature, even though its shape does change. Crystallinity is then understood as responsible for the scatter in the strength-shape relationship, and not the relationship itself. As a result, the strength and shape of the 10 μm silicate feature yield the typical size of the grains in the upper layers of the disk at a few AU from the star (Kessler-Silacci et al. 2007). The top panel of Figure 6.9 shows the results for Serpens, Taurus, Upper Sco and η Cha. The bottom panel presents the median values per region, indicating the 15 – 85 percentile ranges of the distributions. Overlaid are the models of Olofsson et al. (2009) for different grain sizes (0.1 – 6.0 μm) generated for amorphous silicates of olivine and pyroxene stoichiometry, and a 50:50 mixture. The difference in mean ages does not correspond to a significant difference in mean grain sizes between the different regions.

With the mean grain sizes derived from the spectral decomposition, it is possible to further explore the validity of using the strength of the 10 μm silicate feature to trace the sizes of grains in the surfaces of disks. The left panel of Figure 6.10 shows the correlation between $\langle a_{\mathrm{warm}} \rangle$ and $S_{\mathrm{peak}}^{10\mu\mathrm{m}}$ for all 4 samples. The Kendall τ coefficient of -0.29, $P = 0.01$ supports the effectiveness of $S_{\mathrm{peak}}^{10\mu\mathrm{m}}$ as a proxy for grain sizes, with smaller values of $S_{\mathrm{peak}}^{10\mu\mathrm{m}}$ implying larger grain sizes.

On the other hand, it is also possible to test how the degree of crystallinity can influence the strength of the 10 μm silicate feature. The lack of correlation between C_{warm} and $S_{\mathrm{peak}}^{10\mu\mathrm{m}}$ (τ = -0.07, P = 0.14), shown in the right panel of Figure 6.10 for all samples, supports that the degree of crystallinity is not the dominant parameter setting the strength of the 10 μm silicate feature. These results argue against the results of Sargent et al. (2009) that find a high crystallinity fraction and small grains
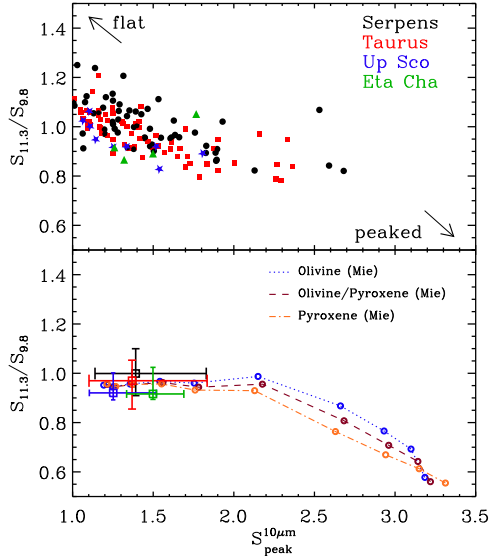
Figure 6.9 – Top: The ratio of normalized fluxes at 11.3 to 9.8 μm ($S_{11.3}/S_{9.8}$) is plotted against the peak at 10 μm ($S_{\mathrm{peak}}^{10\mu\mathrm{m}}$) for Serpens (black dots), Taurus (gray squares), Upper Scorpius (gray stars), η Chamaeleontis (gray triangles). Bottom: Squares show the median values and crosses indicate the 15 – 85 percentile ranges of the distributions (top panel). Colored curves are derived from theoretical opacities for different mixtures by Olofsson et al. (2009). The open circles correspond to different grain sizes, from left to right 6.25, 5.2, 4.3, 3.25, 2.7, 2.0, 1.5, 1.25, 1.0 and 0.1 μm. (A color version of this figure is available in the online journal)
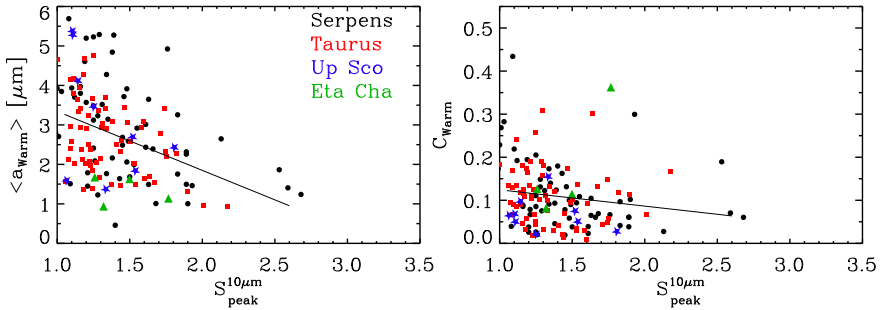
Figure 6.10 – Left panel: Strength of the 10 μm silicate feature ($S_{\mathrm{peak}}^{10\mu\mathrm{m}}$) versus the mass-averaged mean grain size for the warm component. Right panel: Strength of the 10 μm silicate feature versus crystalline fraction for the warm component. The best fit relationships are shown for reference. Symbols as in Figure 6.9. (A color version of this figure is available in the online journal)

fitting low strengths of the 10 μm silicate feature. Although it may be possible to fit a few spectra with a certain prescription, a good model should be able to explain

the robust relationship between the strength and shape of the 10 μm silicate feature observed for large numbers of disks. Despite the many processes able to change the shape or the strength of this feature, only grain size has so far demonstrated capability to explain the observed trend. Our conclusion is that $S_{\mathrm{peak}}^{10\mu\mathrm{m}}$ and dust sizes are appropriately correlated.

6.4.5   Comparison with Other Studies

Dust composition results are available in the literature for the disks in Taurus and η Cha (see Table 6.4 for an overview). Sicilia-Aguilar et al. (2009) present their analysis in η Cha considering the same 5 dust species and three grain sizes (enstatite in their model is the only species for which only the 2 smaller grain sizes are considered), but for a distribution of temperatures derived using the Two Layer Temperature Distribution (TLTD, Juhász et al. 2009) decomposition procedure. For the same 4 objects, their mean amorphous fraction is 80.1 $\pm$ 9.3 %. This result is consistent with the 82.8 $\pm$ 12.9 % mean amorphous fraction found here. The mean crystalline fractions derived are 18.4 $\pm$ 10.7 % with TLTD and 17.1 $\pm$ 12.8 % derived here.

Sargent et al. (2009) present their decomposition procedure for 65 YSOs in Taurus. This method also takes into consideration a warm and a cold temperature, and makes use of two amorphous species (olivine and pyroxene) with two grain sizes (small and large), and 3 crystalline species (enstatite, forsterite and crystalline silica) of a single size. Their mean warm amorphous fraction is 82.9 $\pm$ 19.3 % and warm crystalline fraction is 17.1 $\pm$ 19.3 %, while here the derived fractions are 89.0 $\pm$ 6.6 % and 10.9 $\pm$ 6.6 % for the warm amorphous and crystalline fractions, respectively. For the cold component, Sargent et al. (2009) derive a mean cold amorphous fraction of 77.3 $\pm$ 19.9 % and cold crystalline fraction of 22.6 $\pm$ 19.9 %, while here the values are 85.9 $\pm$ 10.6 % and 13.9 $\pm$ 10.5 %, respectively. The consistently lower amorphous (higher crystalline) fractions found by Sargent et al. (2009) could be a result of their choice to use silica in crystalline rather than amorphous form (as used here).

6.5   Discussion

6.5.1   Dust Characteristics

Section 6.4 has shown that the disk populations in the four regions presented here, young and older, have very similar distributions in the two main dust parameters: grain size and composition. The large number of objects in the two young regions studied occupy a region in parameter space of either grain size or crystallinity fraction that is also populated by the small number of older disks. The grain sizes derived for the cold component never reach the biggest grain size modeled (6 μm), different from the warm component results that span the entire range in sizes. The crystallinity fraction does not seem to be correlated with mean grain size, warm or cold. Whatever processes are responsible for the crystallization of the initially amorphous grains, they should not only be independent from the processes that govern the grain size distribu-

tion, but they should also be able to work on bigger amorphous grains. Alternatively, the crystalline lattice should be able to keep itself regular during the coagulation of small crystalline dust to create big crystalline grains. The correlation between the strength of the 10 μm feature and the mean grain size in disk surfaces, combined with the lack of correlation between crystallinity fraction and $S_{\mathrm{peak}}^{10\mu\mathrm{m}}$, supports the wide usage of $S_{\mathrm{peak}}^{10\mu\mathrm{m}}$ as a proxy for dust size in literature (van Boekel et al. 2003; Kessler-Silacci et al. 2006; Pascucci et al. 2009).

Bouwman et al. (2008) found a strong correlation between disk geometry and the strength of the 10 μm silicate feature for a very small sample of T Tauri stars (7 disks), which points to flatter disks having shallower 10 μm features (i.e., big grains in the disk surface). Using results from similar decomposition procedures, Olofsson et al. (2010) and Juhász et al. (2010) confirm this trend for larger samples of T Tauri (58 disks) and Herbig Ae/Be stars (45 disks), respectively. Those trends are much weaker than that found by Bouwman et al. (2008), showing a larger spread. For the current even larger sample (139 disks), no significant trend is seen, indicating that the earlier small sample trends may have been affected by a few outliers. This result is similar to that found by Oliveira et al. (2010) for a large YSO sample ($\sim$ 200 objects) using the strength of the 10 μm silicate feature as a proxy for grain size (Figure 14 in that paper). As discussed by Oliveira et al., the models of sedimentation only of Dullemond & Dominik (2008) expect a strong correlation of larger grains in flatter disks that is not seen. This means that sedimentation alone cannot be responsible for the distribution of mean grain sizes in the upper layers of protoplanetary disks around T Tauri stars. Furthermore, the lack of correlation between crystallinity fraction and disk geometry is not in support of the results of Watson et al. (2009) and Sargent et al. (2009), who find a link between increasing crystallinity fraction and dust sedimentation.

As discussed in Oliveira et al. (2010) for Serpens and Taurus, and confirmed by the addition of considerably older samples, there is no clear difference in the mean grain sizes in the disk surfaces with mean cluster age, which can be seen in Figure 6.11. This evidence supports the discussion in that paper that the dust population observed in the disk surface cannot be a result of a progressive, monotonic change of state from small amorphous grains, to large, more crystalline grains, or 'grain growth and processing'. The fact that the distribution of grain sizes in the upper layers of disks does not change with cluster age implies that an equilibrium of the processes of dust growth and fragmentation must exist, which also supports the existence of small grains in disks that are millions of years old whereas dust growth is a rapid process (Weidenschilling 1980; Dullemond & Dominik 2005). That small dust is still seen in disks in older regions like Upper Sco and η Cha argues that this equilibrium of processes is maintained for millions of years, as long as the disks are optically thick, but independent of them having a flared or flatter geometry.

Figure 6.11 – Left: Mean mass-average grain sizes vs. disk fraction. Serpens is not included because its disk fraction is not yet known. Filled circles represent mean warm grain sizes, and open triangles represent mean cold grain sizes. Error bars for the mean mass-average grain sizes are estimated using a Monte Carlo approach, sampling the errors of the individual objects. Right: Mean grain sizes vs. mean cluster age. Filled symbols represent results for the warm component, while open symbols represent the cold component. The black points are YSOs in Serpens, gray squares in Taurus, gray stars in Upper Sco and gray triangles in η Cha. (A color version of this figure is available in the online journal)

6.5.2   Evolution of Crystallinity with Time?

Literature studies of disk fractions of different YSO clusters with different mean ages show a trend of decreasing disk fraction, i.e. disks dissipating with time, over some few millions of years (Haisch et al. 2001; Hernández et al. 2008). This decrease is clearly confirmed by the lower fraction of disks still present in the older regions studied here (Upper Sco and η Cha). According to current planet formation theories, if giant planets are to be formed from gas rich disks, the optically thin, gas-poor disks in those older regions should already harbor (proto-)planets. Considering the evidence from small bodies in our own Solar System that suggest considerably higher crystallinity fractions than ISM dust (see Wooden et al. 2007 and Pontoppidan & Brearley 2010 for reviews of latest results), a crystallinity increase must occur.

In Figure 6.12, the mean crystallinity fraction per region is plotted against two evolutionary parameters: disk fraction (left) and mean age (right). Within the spread in individual fractions it is seen that, just as for grain sizes, there is no strong evidence of an increase of crystallinity fraction with either evolutionary parameter. This implies that there is no evolution in grain sizes or crystallinity fraction for the dust in the surface of disks over cluster ages in the range 1 – 8 Myr, as probed by the observations presented here. Essentially, there is no change in these two parameters until the disks disperse. Starting from the assumption that initially the dust in protoplanetary disks is of ISM origin (sub-μm in size and almost completely amorphous), it appears that a modest level of crystallinity is established in the disk surface early in the evolution (≤ 1 Myr) and then reaches some sort of steady state, irrespective of what is taking place in the disk midplane. Thus, the dust in the upper layers of disks does not seem to be a good tracer of the evolution that is taking place in the disk interior, where dust is
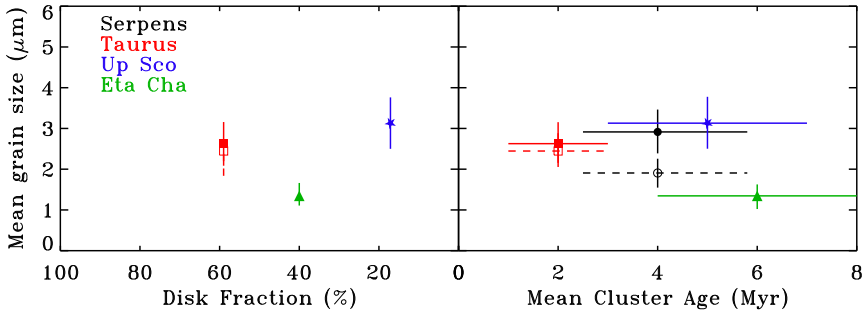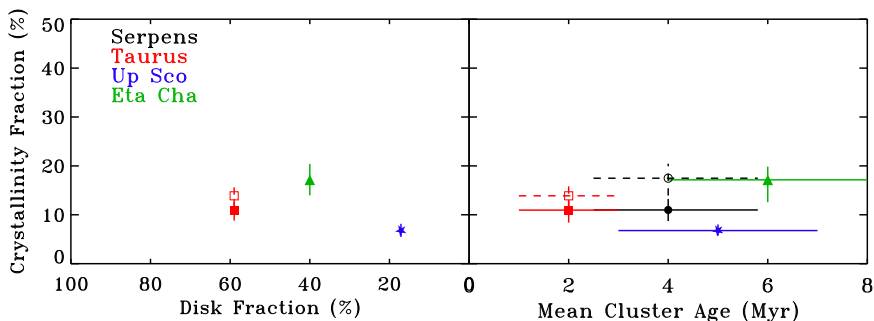
Figure 6.12 − Left: Crystallinity fraction vs. disk fraction. Serpens is not included because its disk fraction is not yet known. Filled circles represent mean warm crystallinity, and open triangles represent mean cold crystallinity. Uncertainty for crystallinity fractions are estimated using a Monte Carlo approach, sampling the errors of the individual objects. Right: Crystallinity fraction vs. mean cluster age. Filled symbols represent results for the warm component, while open symbols represent the cold component. The black points are YSOs in Serpens, gray squares in Taurus, gray stars in Upper Sco and gray triangles in η Cha. (A color version of this figure is available in the online journal)

growing further for the formation of planetesimals and planets, at many times higher crystallinity fractions, to be consistent with evidence from Solar system bodies.

If this is the case, within 1 Myr this surface dust must be crystallized to the observed fraction ($\sim$10 – 20 %). This result puts constraints on the formation of circumstellar disks. One possibility is that this crystallization of the dust in disks mostly occurs during the embedded phase. In this early stage of star formation, where large quantities of material are still accreting towards the protostar, a fraction of the infalling material comes very close to the protostar and is heated to temperatures >800 K before it moves outwards in the disk. Alternatively, accretion shocks or episodic heating events could be responsible for thermally annealing the dust in the disk surface.

The 2-D models of Visser & Dullemond (2010) treat the radial evolution of crystals in time. According to these models, 100 % of the dust in the inner disk ($\leq$ 1 AU) is crystallized within 1 Myr. With time, the inner disk crystalline fraction drops as the disk spreads, and crystalline material is transported to outer parts of the disk. These models can help explain the rapid crystallization required to account for our results. However, the models do show a decrease in inner disk ($\leq$ 1 AU) crystallinity fraction with time, which is not supported by our results. Since these models do not discriminate on vertical structure, but rather present crystallinity fractions that are integrated over all heights at a given radius, this decrease in crystallinity fraction is not necessarily connected to the surface of the disk. Thus the decrease in crystallinity fraction with time found in the models of Visser & Dullemond (2010) could be explained as a decrease in crystallinity fraction just in the disk midplane where the bulk of the mass resides, but not in the surface layers, as our data indicate. That would

imply that radial mixing of these crystals is more efficient than vertical mixing, which is responsible for the crystallinity fraction decrease in the disk midplane.

According to the models of Ciesla (2007) for outward transport of high temperature materials, variations in radial transport dynamics with height produce vertical gradients in the crystalline fractions, such that the upper layers of the disk will have lower crystallinity fractions than the midplane population. If that is the case, the observations discussed here, which probe the disk surface only, lead to lower limits on the real crystalline fraction of disk midplanes. In this scenario, planets (and comets) forming in the disk midplane would have higher crystalline abundances than those derived here for the disk surfaces, which are compatible with what has been observed in our Solar System. However, this model does not make predictions for the time evolution of the systems. Combining the vertical and radial mixing processes with evolutionary models such as those of Visser & Dullemond (2010) are needed to investigate whether older and younger disks could still show the same distribution of crystallinity fractions in the upper layers of disks, as observed here.

6.6   Conclusions

This paper presents the spectral decomposition of Spitzer/IRS spectra using the B2C decomposition model of Olofsson et al. (2010). Mineralogical compositions and size distributions of dust grains in the surface layers of protoplanetary disks are derived for 139 YSOs belonging to four young star clusters using the same method.

Serpens and Taurus are used as prototypes of young regions, where most stars are still surrounded by disks, while Upper Sco and η Cha represent the older bin of disk evolution, where a large fraction of the disks have already dissipated but some massive protoplanetary disks are left. The large number of objects analyzed allows statistical results that point to the main processes that affect the grain size distribution and composition of dust in protoplanetary disks. Furthermore, the usage of the same analysis method for regions of different mean ages allow a study of evolution of the dust parameters with time.

Our large sample does not show a preferential grain size or crystallinity fraction with disk geometry, contrary to earlier analyses based on smaller samples. Also, younger and older regions have very similar distributions. The difference between mean mass-averaged grain sizes for the warm and cold components of a given star-forming region is small, however a considerable difference is seen between the ranges of grain sizes spanned in both components. The cold mass-averaged grain sizes never reach the biggest size modelled (6 μm) while the warm mass-averaged grain sizes span the entire range of sizes modeled. The crystallinity fractions derived for inner (warm) and outer (cold) disks are typically 10 – 20%, and not correlated. The cold crystallinity fraction shows a larger spread than the warm. No strong difference is seen between the overall mean warm and cold crystallinity fraction. Within the crystalline dust population, more enstatite is found in the warm component and more forsterite in the cold component. The differences are not very significant, however.

The results of the spectral decomposition support the usage of the strength of the 10 μm silicate feature ($S_{\mathrm{peak}}^{10\mu\mathrm{m}}$) as a proxy of the mean grain size of dust in the disk surface. This is supported by the correlation between $S_{\mathrm{peak}}^{10\mu\mathrm{m}}$ and mean grain size and lack of correlation with the mean crystallinity.

Mean cluster ages and disk fractions are used as indicators of the evolutionary stage of the different populations. Our results show that the different regions have similar distributions of mean grain sizes and crystallinity fractions regardless of the spread in mean ages of $1 - 8$ Myr. Thus, despite the fact that the majority of disks dissipate within a few Myr, the surface dust properties do not depend on age for those disks that have not yet dissipated in the $1 - 8$ Myr range. This points to a rapid change in the composition and crystallinity of the dust in the early stages (≤ 1 Myr) that is maintained essentially until the disks dissipate.

References

Ábrahám, P., et al. 2009, Nature, 459, 224

Apai, D., Pascucci, I., Bouwman, J., Natta, A., Henning, T., & Dullemond, C. P. 2005, Science, 310, 834

Beckwith, S. V. W., Henning, T., & Nakagawa, Y. 2000, Protostars and Planets IV, 533

Beichman, C. A., et al. 2006, ApJ, 639, 1166

Blaauw, A. 1978, Problems of Physics and Evolution of the Universe, 101

Bockelée-Morvan, D., et al. 2000, A&A, 353, 1101

Bouwman, J., Meeus, G., de Koter, A., Hony, S., Dominik, C., & Waters, L. B. F. M. 2001, A&A, 375, 950

Bouwman, J., et al. 2008, ApJ, 683, 479

Bouy, H., et al. 2008, A&A, 486, 877

Brown, J. M., et al. 2007, ApJ, 664, L107

Bryden, G., et al. 2006, ApJ, 636, 1098

Carpenter, J. M., Mamajek, E. E., Hillenbrand, L. A., & Meyer, M. R. 2006, ApJ, 651, L49

Carpenter, J. M., et al. 2009, ApJS, 181, 197

Ciesla, F. J. 2007, Science, 318, 613

Ciesla, F. J. 2009, Icarus, 200, 655

Crovisier, J., Leech, K., Bockelee-Morvan, D., Brooke, T. Y., Hanner, M. S., Altieri, B., Keller, H. U., & Lellouch, E. 1997, Science, 275, 1904

Dahm, S. E., & Carpenter, J. M. 2009, AJ, 137, 4024

Desch, S. J., & Connolly, H. C., Jr. 2002, Meteoritics and Planetary Science, 37, 183

de Zeeuw, P. T., Hoogerwerf, R., de Bruijne, J. H. J., Brown, A. G. A., & Blaauw, A. 1999, AJ, 117, 354

Dullemond, C. P., Dominik, C., & Natta, A. 2001, ApJ, 560, 957

Dullemond, C. P., & Dominik, C. 2005, A&A, 434, 971

Dullemond, C. P., & Dominik, C. 2008, A&A, 487, 205

Dzib, S., Loinard, L., Mioduszewski, A. J., Boden, A. F., Rodríguez, L. F., & Torres, R. M. 2010, ApJ, 718, 610

Fabian, D., Jäger, C., Henning, T., Dorschner, J., & Mutschke, H. 2000, A&A, 364, 282

Forrest, W. J., et al. 2004, ApJS, 154, 443

Furlan, E., et al. 2006, ApJS, 165, 568

Gail, H.-P. 2004, A&A, 413, 571

Gautier, T. N., III, et al. 2007, ApJ, 667, 527

Geers, V. C., et al. 2006, A&A, 459, 545

Haisch, K. E., Jr., Lada, E. A., & Lada, C. J. 2001, ApJ, 553, L153

Harker, D. E., & Desch, S. J. 2002, ApJ, 565, L109

Harker, D. E., Wooden, D. H., Woodward, C. E., & Lisse, C. M. 2002, ApJ, 580, 579

Harker, D. E., Woodward, C. E., & Wooden, D. H. 2005, Science, 310, 278

Harker, D. E., Woodward, C. E., Wooden, D. H., Fisher, R. S., & Trujillo, C. A. 2007, Icarus, 190, 432

Hartmann, L., Ballesteros-Paredes, J., & Bergin, E. A. 2001, ApJ, 562, 852

Henning, T. 2010, ARA&A, 48, 21

Hernández, J., Hartmann, L., Calvet, N., Jeffries, R. D., Gutermuth, R., Muzerolle, J., & Stauffer, J. 2008, ApJ, 686, 1195

Houck, J. R., et al. 2004, ApJS, 154, 18

Juhász, A., Henning, T., Bouwman, J., Dullemond, C. P., Pascucci, I., & Apai, D. 2009, ApJ, 695, 1024

Juhász, A., et al. 2010, ApJ, 721, 431

Kalas, P., et al. 2008, Science, 322, 1345

Kemper, F., Vriend, W. J., & Tielens, A. G. G. M. 2004, ApJ, 609, 826

Kenyon, S. J., & Hartmann, L. 1987, ApJ, 323, 714

Kenyon, S. J., Dobrzycka, D., & Hartmann, L. 1994, AJ, 108, 1872

Kessler-Silacci, J., et al. 2006, ApJ, 639, 275

Kessler-Silacci, J. E., et al. 2007, ApJ, 659, 680

Kóspál, Á., Ardila, D. R., Moór, A., & Ábrahám, P. 2009, ApJ, 700, L73

Lagrange, A.-M., et al. 2010, Science, 329, 57

Lahuis, F., Kessler-Silacci, J. E., Evans, N. J., I., et al. 2006, c2d Spectroscopy Explanatory Supplement, Tech. rep., Pasadena: Spitzer Science Center

Li, A., & Draine, B. T. 2001, ApJ, 550, L213

Lisse, C. M., Kraemer, K. E., Nuth, J. A., Li, A., & Joswiak, D. 2007, Icarus, 187, 69

Lisse, C. M., Chen, C. H., Wyatt, M. C., & Morlok, A. 2008, ApJ, 673, 1106

Luhman, K. L., & Steeghs, D. 2004, ApJ, 609, 917

Luhman, K. L., Allen, P. R., Espaillat, C., Hartmann, L., & Calvet, N. 2010, ApJS, 186, 111

Malfait, K., Waelkens, C., Waters, L. B. F. M., Vandenbussche, B., Huygen, E., & de Graauw, M. S. 1998, A&A, 332, L25x

Mamajek, E. E., Lawson, W. A., & Feigelson, E. D. 1999, ApJ, 516, L77

Megeath, S. T., Hartmann, L., Luhman, K. L., & Fazio, G. G. 2005, ApJ, 634, L113

Meeus, G., Waters, L. B. F. M., Bouwman, J., van den Ancker, M. E., Waelkens, C., & Malfait, K. 2001, A&A, 365, 476

Merín, B., et al. 2007, ApJ, 661, 361

Merín, B., et al. 2010, ApJ, 718, 1200

Min, M., Hovenier, J. W., & de Koter, A. 2005, A&A, 432, 909

Min, M., Hovenier, J. W., de Koter, A., Waters, L. B. F. M., & Dominik, C. 2005, Icarus, 179, 158

Min, M., Waters, L. B. F. M., de Koter, A., Hovenier, J. W., Keller, L. P., & Markwick-Kemper, F. 2007, A&A, 462, 667

Min, M., Hovenier, J. W., Waters, L. B. F. M., & de Koter, A. 2008, A&A, 489, 135

Oliveira, I., et al. 2009, ApJ, 691, 672

Oliveira, I., et al. 2010, ApJ, 714, 778

Olofsson, J., et al. 2009, A&A, 507, 327

Olofsson, J., Augereau, J.-C., van Dishoeck, E. F., Merín, B., Grosso, N., Ménard, F., Blake, G. A., & Monin, J.-L. 2010, A&A, 520, A39

Pascucci, I., Apai, D., Luhman, K., Henning, T., Bouwman, J., Meyer, M. R., Lahuis, F., & Natta, A. 2009, ApJ, 696, 143

Pinte, C., et al. 2008, A&A, 489, 633

Pontoppidan, K. M., & Brearley, A. J. 2010, Protoplanetary Dust: Astrophysical and Cosmochemical Perspectives, 191

Rieke, G. H., et al. 2005, ApJ, 620, 1010

Sargent, B. A., et al. 2009, ApJS, 182, 477

Sicilia-Aguilar, A., et al. 2009, ApJ, 701, 1188

Schegerer, A. A., Wolf, S., Ratzka, T., & Leinert, C. 2008, A&A, 478, 779

Straizys, V., Cernis, K. & Bartasiute, S. 1996, Baltic Astron., 5, 125

Su, K. Y. L., et al. 2006, ApJ, 653, 675

Udry, S., & Santos, N. C. 2007, ARA&A, 45, 397

van Boekel, R., Waters, L. B. F. M., Dominik, C., Bouwman, J., de Koter, A., Dullemond, C. P., & Paresce, F. 2003, A&A, 400, L21

van Boekel, R., et al. 2004, Nature, 432, 479

van Boekel, R., Min, M., Waters, L. B. F. M., de Koter, A., Dominik, C., van den Ancker, M. E., & Bouwman, J. 2005, A&A, 437, 189

Visser, R., & Dullemond, C. P. 2010, A&A, 519, A28

Watson, D. M., et al. 2009, ApJS, 180, 84

Weidenschilling, S. J. 1980, Icarus, 44, 172

Wooden, D. H., Harker, D. E., Woodward, C. E., Butner, H. M., Koike, C., Witteborn, F. C., & McMurtry, C. W. 1999, ApJ, 517, 1034

Wooden, D., Desch, S., Harker, D., Gail, H.-P., & Keller, L. 2007, Protostars and Planets V, 815

Zolensky, M. E., et al. 2006, Science, 314, 1735

Table 6.1 – Characteristics of the star-forming regions presented in this work.

Region	Dist (pc)	Mean Age (Myr)	Disk Fraction	Ref.
Serpens	259–415	2–6	–	1, 2
Taurus	140	∼2	∼60%	3, 4, 5
Up Sco	145	∼5	∼17%	6, 7, 8
η Cha	97	∼6	∼40%	9, 10, 11

References: **1**: The distance to Serpens is still under debate, different methods yield distances ranging from 259 (Straizys et al. 1996) to 415 pc (Dzib et al. 2010); **2**: From Oliveira et al. (2009), using $d = 259$ pc; **3**: From Kenyon et al. (1994); **4**: From Hartmann et al. (2001); **5**: From Luhman et al. (2010); **6**: From de Zeeuw et al. (1999); **7**: From Blaauw (1978); **8**: From Carpenter et al. (2006); **9**: From Mamajek et al. (1999); **10**: From Luhman & Steeghs (2004); **11**: From Megeath et al. (2005).

Table 6.2 – B2C mean composition of each star-forming region.

Region	Oli/Pyr[a]	Silica	Forsterite	Enstatite
		Warm	Component	
Serpens	81.3±11.7%	7.8±6.5%	5.8±4.9%	5.2±4.9%
Taurus	79.4±9.4%	9.6±7.0%	4.4±3.3%	6.5±4.5%
Up Sco	89.7±4.7%	3.5±3.4%	2.6±1.1%	4.1±3.1%
η Cha	75.0±13.4%	7.8±4.6%	6.8±4.0%	10.3±9.8%
		Cold	Component	
Serpens	68.0±20.1%	14.4±12.3%	9.5±9.5%	8.0±8.0%
Taurus	64.7±14.3%	21.3±11.4%	8.6±8.6%	5.3±5.3%

[a] Amorphous olivine and pyroxene combined.

Table 6.3 – B2C mean grain size and crystallinity parameters for each star-forming region.

Region	Number	$\langle a_{\text{warm}} \rangle$ μm	$\langle a_{\text{cold}} \rangle$ μm	$\langle \alpha_{\text{warm}} \rangle$	$\langle \alpha_{\text{cold}} \rangle$	$\langle C_{\text{warm}} \rangle$ %	$\langle C_{\text{cold}} \rangle$ %
Serpens	60	2.9±1.3	1.9±0.6	-2.75±0.39	-3.16±0.18	11.0±6.9	17.5±12.4
Taurus	66	2.6±0.9	2.4±0.6	-2.83±0.31	-3.02±0.15	10.9±5.6	13.9±10.1
Up Sco	9	3.1±1.5	–	-3.33±0.18	–	6.8±3.3	–
η Cha	4	1.3±0.4	–	-2.71±0.39	–	17.1±10.6	–

Table 6.4 – Comparison of mean mineralogical results from this study with literature studies.

Region	This	work	Literature	
	Amorphous	Crystalline	Amorphous	Crystalline
		Warm	Component	
Taurus	89.0±6.6 %	10.9±6.6 %	82.9±19.3 %	17.1±19.3 % [a]
η Cha	82.8±12.9 %	17.1±12.8 %	80.1±9.3 %	18.4±10.7 % [b]
		Cold	Component	
Taurus	85.9±10.6 %	13.9±10.5 %	77.3±19.9 %	22.6±19.9 % [a]

[a] Sargent et al. (2009); [b] Sicilia-Aguilar et al. (2009)

A. Relative Abundances of Species

The relative abundances, as resulting from the B2C compositional fitting (§ 6.3) to the IRS spectra of protoplanetary disks in Serpens, Taurus, Upper Sco and η Cha are shown in Tables A.1 and A.2. Since the opacities of amorphous olivine and pyroxene are degenerate, the abundances of these two species have been added into one, marked 'Oli/Pyr' in the Tables. Furthermore, 'Sil' designates the amorphous silica, and the crystalline enstatite and forsterite are marked as 'Ens' and 'For', respectively. In the tables, the first line of a given object corresponds to the results of the fit to the warm component and the second line to the results of the cold component. For some objects (20 in Serpens, 28 in Taurus, all in Upper Sco and η Cha), the S/N drops considerably at longer wavelengths and the results of the procedure are no longer reliable. For these sources, the cold component could not be fitted satisfactorily and, in Tables A.1 and A.2, only the warm component results are shown.

ID	SpT	Oli/Pyr[a] % (0.1 μm)	Ens % (0.1 μm)	For % (0.1 μm)	Sil % (0.1 μm)
Serpens					
1	K2	$29.7^{+10.7}_{-15.3}$	$1.0^{+2.0}_{-0.4}$	$2.6^{+2.6}_{-1.4}$	$0.1^{+0.9}_{-0.0}$
...		$38.4^{+14.5}_{-15.8}$	$0.0^{+1.6}_{-0.0}$	$8.7^{+5.5}_{-3.6}$	$1.2^{+3.0}_{-0.0}$
3	M0	$26.5^{+15.9}_{-7.3}$	$0.0^{+2.4}_{-0.0}$	$0.9^{+3.5}_{-0.4}$	$0.0^{+1.7}_{-0.0}$
...		$27.3^{+33.7}_{-8.6}$	$0.0^{+10.5}_{-0.0}$	$10.2^{+19.1}_{-4.9}$	$0.0^{+16.3}_{-4.0}$
6	K5	$25.4^{+4.5}_{-6.0}$	$0.0^{+0.7}_{-0.0}$	$0.8^{+1.1}_{-0.0}$	$0.0^{+0.3}_{-0.0}$
...		$6.4^{+3.8}_{-3.3}$	$4.1^{+2.1}_{-2.3}$	$5.1^{+3.4}_{-0.0}$	$0.5^{+1.1}_{-0.0}$
7	M0	$3.7^{+3.1}_{-0.9}$	$0.0^{+2.9}_{-0.0}$	$0.8^{+4.3}_{-0.0}$	$0.0^{+0.9}_{-0.0}$
...		$0.0^{+3.4}_{-0.5}$	$7.2^{+4.9}_{-6.9}$	$8.1^{+5.3}_{-6.9}$	$14.1^{+8.3}_{-11.5}$
9	–	$58.3^{+10.9}_{-8.8}$	$0.0^{+1.4}_{-0.0}$	$0.5^{+1.1}_{-0.0}$	$0.0^{+0.7}_{-0.0}$
...		$24.5^{+16.3}_{-14.5}$	$0.0^{+3.5}_{-0.0}$	$14.4^{+13.9}_{-9.8}$	$16.9^{+24.0}_{-15.0}$
10	–	$1.9^{+5.9}_{-0.6}$	$0.0^{+2.5}_{-0.0}$	$2.3^{+2.1}_{-0.7}$	$4.3^{+2.4}_{-1.4}$
...		$37.4^{+29.1}_{-9.4}$	$2.0^{+10.1}_{-0.0}$	$0.0^{+9.2}_{-0.0}$	$0.0^{+19.4}_{-0.0}$
14	M2	$11.1^{+46.8}_{-0.0}$	$0.0^{+6.0}_{-0.0}$	$3.0^{+7.1}_{-0.0}$	$0.0^{+6.9}_{-0.0}$
15	–	$35.6^{+12.5}_{-7.0}$	$0.2^{+1.5}_{-0.0}$	$2.9^{+1.6}_{-1.3}$	$0.0^{+0.6}_{-0.0}$
...		$36.3^{+10.4}_{-12.9}$	$2.4^{+1.8}_{-1.6}$	$2.2^{+3.5}_{-0.0}$	$1.1^{+2.8}_{-0.9}$
21	–	$2.2^{+5.0}_{-0.0}$	$0.0^{+1.6}_{-0.0}$	$2.7^{+3.7}_{-0.0}$	$0.1^{+3.6}_{-0.0}$
...		$33.0^{+18.1}_{-20.7}$	$1.6^{+5.2}_{-0.0}$	$0.0^{+2.3}_{-0.0}$	$1.3^{+11.9}_{-0.0}$
29	M2	$1.4^{+6.4}_{-0.0}$	$0.0^{+3.1}_{-0.0}$	$1.6^{+7.8}_{-0.0}$	$2.7^{+6.6}_{-0.0}$
30	M1	$0.0^{+9.7}_{-0.0}$	$0.1^{+4.4}_{-0.0}$	$3.4^{+4.6}_{-1.2}$	$4.5^{+6.8}_{-0.2}$
...		$10.3^{+51.7}_{-13.8}$	$1.7^{+15.4}_{-3.2}$	$5.5^{+14.1}_{-4.3}$	$8.1^{+21.6}_{-6.3}$
31	–	$1.2^{+0.8}_{-0.0}$	$0.0^{+0.8}_{-0.0}$	$0.8^{+0.5}_{-0.0}$	$0.0^{+1.0}_{-0.0}$
...		$21.8^{+5.3}_{-4.9}$	$2.4^{+1.6}_{-0.0}$	$0.0^{+0.7}_{-0.0}$	$16.7^{+8.7}_{-7.9}$
36	K5	$22.3^{+5.2}_{-6.2}$	$0.9^{+1.6}_{-0.0}$	$0.6^{+1.3}_{-0.0}$	$0.0^{+0.8}_{-0.0}$
...		$37.4^{+11.0}_{-15.4}$	$0.0^{+3.9}_{-0.0}$	$1.6^{+2.7}_{-1.0}$	$2.9^{+8.6}_{-2.5}$

ID	SpT	Oli/Pyr[a] % (0.1 μm)	Ens % (0.1 μm)	For % (0.1 μm)	Sil % (0.1 μm)
40	M7	$0.0^{+8.3}_{-0.0}$	$0.0^{+8.4}_{-0.0}$	$2.9^{+4.4}_{-0.8}$	$10.9^{+4.6}_{-4.1}$
...		$24.2^{+15.5}_{-18.3}$	$16.6^{+11.2}_{-8.4}$	$3.1^{+16.4}_{-0.0}$	$0.0^{+4.8}_{-0.0}$
41	K2	$0.0^{+18.9}_{-0.0}$	$6.3^{+19.1}_{-0.0}$	$3.9^{+16.0}_{-0.0}$	$0.8^{+8.6}_{-0.0}$
43	M0.5	$0.0^{+13.0}_{-0.0}$	$0.0^{+4.0}_{-0.0}$	$4.2^{+5.7}_{-0.0}$	$4.6^{+6.1}_{-0.0}$
48	M5.5	$7.0^{+17.5}_{-0.1}$	$0.1^{+8.4}_{-0.0}$	$2.0^{+10.2}_{-0.0}$	$0.6^{+3.0}_{-0.6}$
...		$46.0^{+23.9}_{-40.6}$	$5.1^{+10.9}_{-3.3}$	$2.5^{+10.5}_{-1.1}$	$0.3^{+21.3}_{-2.3}$
53	M2.5	$0.0^{+36.7}_{-0.0}$	$5.0^{+26.6}_{-0.0}$	$5.4^{+18.5}_{-0.0}$	$5.9^{+20.1}_{-0.0}$
55	K2	$16.9^{+11.3}_{-4.0}$	$1.6^{+2.7}_{-0.9}$	$2.3^{+2.5}_{-0.0}$	$0.0^{+1.1}_{-0.0}$
...		$27.7^{+81.3}_{-23.1}$	$4.8^{+36.6}_{-1.1}$	$21.5^{+34.7}_{-14.2}$	$0.0^{+22.9}_{-0.0}$
56	–	$7.8^{+8.3}_{-2.0}$	$1.7^{+1.9}_{-0.8}$	$2.5^{+2.4}_{-0.0}$	$1.1^{+3.4}_{-0.0}$
...		$44.4^{+22.2}_{-17.0}$	$1.6^{+5.1}_{-1.0}$	$0.0^{+6.4}_{-0.0}$	$2.2^{+21.1}_{-0.0}$
57	–	$2.2^{+22.8}_{-0.0}$	$0.0^{+9.1}_{-0.0}$	$5.7^{+7.2}_{-1.1}$	$3.0^{+3.2}_{-1.4}$
...		$23.0^{+76.9}_{-5.8}$	$0.0^{+79.5}_{-0.0}$	$14.4^{+46.6}_{-10.4}$	$0.7^{+131.2}_{-0.0}$
58	K7	$6.6^{+3.2}_{-0.5}$	$0.0^{+1.0}_{-0.0}$	$0.6^{+1.1}_{-0.0}$	$1.2^{+0.7}_{-0.0}$
...		$32.2^{+16.8}_{-16.4}$	$3.2^{+15.6}_{-0.0}$	$0.0^{+3.7}_{-0.0}$	$0.0^{+7.2}_{-0.0}$
60	M0.5	$0.0^{+10.1}_{-0.0}$	$9.8^{+23.2}_{-0.0}$	$5.2^{+11.8}_{-0.0}$	$0.0^{+3.9}_{-0.0}$
61	M0	$12.2^{+7.2}_{-0.0}$	$0.0^{+0.6}_{-0.0}$	$1.8^{+1.3}_{-0.0}$	$0.0^{+1.1}_{-0.0}$
...		$38.2^{+3.7}_{-7.6}$	$0.0^{+0.8}_{-0.0}$	$0.1^{+0.9}_{-0.0}$	$0.6^{+1.7}_{-0.0}$
65	–	$0.0^{+2.7}_{-0.0}$	$0.0^{+2.0}_{-0.0}$	$6.0^{+2.6}_{-2.5}$	$0.0^{+1.0}_{-0.0}$
...		$54.9^{+56.6}_{-19.1}$	$0.1^{+7.9}_{-0.0}$	$0.0^{+6.3}_{-0.0}$	$8.8^{+16.2}_{-6.6}$
66	K5	$2.1^{+8.1}_{-0.0}$	$0.0^{+1.6}_{-0.0}$	$0.1^{+1.5}_{-0.0}$	$0.8^{+2.4}_{-0.0}$
...		$33.5^{+10.5}_{-16.5}$	$3.9^{+16.1}_{-0.0}$	$4.2^{+14.3}_{-0.0}$	$0.0^{+4.9}_{-0.0}$
71	M3	$6.4^{+28.2}_{-0.0}$	$0.0^{+1.8}_{-0.0}$	$2.3^{+6.8}_{-0.0}$	$0.8^{+8.7}_{-0.0}$
74	–	$0.0^{+5.1}_{-0.0}$	$0.0^{+1.7}_{-0.0}$	$6.3^{+3.7}_{-2.8}$	$13.4^{+4.8}_{-6.3}$
...		$50.7^{+33.8}_{-19.5}$	$0.1^{+11.1}_{-0.0}$	$0.1^{+6.4}_{-0.0}$	$0.0^{+29.4}_{-0.0}$
75	–	$0.0^{+72.5}_{-0.0}$	$0.0^{+10.2}_{-0.0}$	$4.1^{+28.5}_{-0.0}$	$0.1^{+20.2}_{-0.0}$
76	M1	$5.3^{+9.6}_{-3.4}$	$0.0^{+2.8}_{-0.0}$	$2.6^{+3.3}_{-0.0}$	$1.9^{+3.1}_{-0.0}$
...		$41.8^{+17.5}_{-23.6}$	$3.6^{+4.5}_{-1.9}$	$0.0^{+3.3}_{-0.0}$	$0.0^{+2.8}_{-0.0}$
80	–	$0.3^{+1.2}_{-0.0}$	$0.0^{+0.2}_{-0.0}$	$1.2^{+0.5}_{-0.0}$	$0.0^{+0.4}_{-0.0}$
...		$6.4^{+50.4}_{-0.0}$	$8.3^{+29.8}_{-0.0}$	$0.6^{+12.4}_{-0.0}$	$7.4^{+34.2}_{-0.0}$
81	M5	$10.7^{+2.8}_{-0.0}$	$0.0^{+0.8}_{-0.0}$	$0.0^{+0.4}_{-0.0}$	$4.3^{+1.2}_{-0.0}$
...		$45.4^{+6.2}_{-5.1}$	$0.0^{+1.1}_{-0.0}$	$0.0^{+0.4}_{-0.0}$	$0.0^{+1.5}_{-0.0}$
86	M5.5	$15.7^{+3.1}_{-1.7}$	$0.0^{+0.5}_{-0.0}$	$0.8^{+0.7}_{-0.0}$	$0.0^{+0.2}_{-0.0}$
...		$26.7^{+83.1}_{-0.0}$	$12.2^{+28.5}_{-0.0}$	$0.0^{+38.4}_{-0.0}$	$1.9^{+14.8}_{-0.0}$
88	M0.5	$0.0^{+5.0}_{-0.0}$	$0.0^{+1.0}_{-0.0}$	$8.6^{+4.4}_{-0.0}$	$0.0^{+0.4}_{-0.0}$
...		$6.0^{+30.9}_{-10.0}$	$0.7^{+37.8}_{-9.0}$	$33.3^{+22.2}_{-13.7}$	$6.0^{+31.7}_{-9.2}$
89	K5	$0.0^{+0.7}_{-0.0}$	$0.0^{+0.2}_{-0.0}$	$2.6^{+1.6}_{-1.0}$	$1.6^{+0.7}_{-0.0}$
90	–	$26.0^{+20.9}_{-12.1}$	$0.0^{+4.1}_{-0.1}$	$3.0^{+4.4}_{-1.6}$	$0.0^{+2.7}_{-0.0}$
...		$31.1^{+65.4}_{-0.0}$	$7.5^{+13.4}_{-1.4}$	$8.5^{+51.3}_{-0.0}$	$0.7^{+21.3}_{-0.0}$
92	M0	$1.1^{+9.7}_{-0.0}$	$0.0^{+0.9}_{-0.0}$	$4.8^{+4.8}_{-0.0}$	$2.3^{+5.3}_{-0.1}$
...		$19.6^{+9.7}_{-7.1}$	$0.8^{+3.4}_{-0.0}$	$0.2^{+9.0}_{-0.0}$	$3.0^{+4.6}_{-0.0}$

ID	SpT	Oli/Pyr[a] % (0.1 μm)	Ens % (0.1 μm)	For % (0.1 μm)	Sil % (0.1 μm)
96	M1	$18.2^{+8.7}_{-11.8}$	$2.6^{+3.8}_{-2.0}$	$2.8^{+4.6}_{-1.6}$	$0.0^{+5.9}_{-0.0}$
100	–	$0.0^{+29.3}_{-0.0}$	$0.0^{+12.0}_{-0.0}$	$2.8^{+42.3}_{-0.0}$	$0.5^{+35.5}_{-0.0}$
101	–	$24.1^{+26.6}_{-6.9}$	$0.0^{+4.1}_{-0.0}$	$2.0^{+3.2}_{-1.4}$	$1.0^{+4.2}_{-0.0}$
...		$48.0^{+7.1}_{-19.8}$	$0.0^{+2.7}_{-0.1}$	$0.2^{+2.7}_{-0.0}$	$2.5^{+3.1}_{-1.9}$
103	–	$0.0^{+0.9}_{-0.0}$	$0.0^{+0.3}_{-0.0}$	$2.4^{+0.6}_{-0.0}$	$3.2^{+0.9}_{-0.0}$
...		$11.0^{+3.7}_{-9.1}$	$5.8^{+4.2}_{-2.7}$	$0.0^{+3.9}_{-0.0}$	$5.8^{+3.3}_{-1.8}$
104	–	$1.6^{+14.7}_{-1.1}$	$0.9^{+6.1}_{-0.2}$	$3.7^{+5.2}_{-2.3}$	$4.3^{+4.1}_{-1.8}$
106	M3	$0.0^{+16.0}_{-0.0}$	$5.1^{+23.7}_{-0.0}$	$4.0^{+17.1}_{-0.0}$	$5.7^{+34.2}_{-0.0}$
113	K7	$0.0^{+1.2}_{-0.0}$	$0.0^{+0.7}_{-0.0}$	$3.3^{+1.7}_{-0.5}$	$4.4^{+1.3}_{-1.9}$
...		$36.9^{+19.9}_{-14.1}$	$2.1^{+8.1}_{-0.0}$	$3.6^{+4.2}_{-1.4}$	$0.0^{+2.6}_{-0.0}$
114	F9	$0.4^{+5.3}_{-0.0}$	$0.0^{+0.5}_{-0.0}$	$2.8^{+1.2}_{-1.1}$	$0.1^{+0.8}_{-0.0}$
115	M0.5	$3.5^{+6.8}_{-2.2}$	$0.4^{+1.2}_{-0.2}$	$1.5^{+1.5}_{-0.0}$	$0.6^{+1.2}_{-0.0}$
117	K2	$74.6^{+32.8}_{-31.9}$	$1.4^{+3.6}_{-0.0}$	$5.9^{+2.1}_{-4.1}$	$0.0^{+1.6}_{-0.0}$
...		$37.9^{+14.9}_{-15.7}$	$6.3^{+5.5}_{-4.7}$	$19.0^{+9.2}_{-9.9}$	$6.1^{+5.3}_{-4.1}$
119	K7	$0.0^{+11.2}_{-0.0}$	$0.7^{+23.7}_{-0.0}$	$1.1^{+17.4}_{-0.0}$	$1.9^{+31.6}_{-0.0}$
122	M0	$30.7^{+3.5}_{-30.4}$	$0.0^{+7.8}_{-0.0}$	$1.4^{+10.5}_{-0.0}$	$0.0^{+7.1}_{-0.0}$
...		$25.3^{+38.5}_{-12.9}$	$0.2^{+7.5}_{-0.6}$	$5.5^{+19.7}_{-0.0}$	$22.7^{+36.9}_{-14.1}$
123	M0	$42.0^{+65.0}_{-19.7}$	$0.7^{+3.3}_{-0.0}$	$5.4^{+2.7}_{-3.7}$	$0.0^{+1.4}_{-0.0}$
125	M0	$4.9^{+13.0}_{-0.0}$	$0.0^{+3.3}_{-0.0}$	$2.3^{+2.5}_{-1.6}$	$0.0^{+1.9}_{-0.0}$
...		$31.0^{+10.3}_{-20.4}$	$11.6^{+1.5}_{-12.8}$	$0.0^{+0.9}_{-2.6}$	$0.0^{+2.5}_{-0.0}$
127	M2	$1.5^{+2.9}_{-0.0}$	$3.4^{+1.2}_{-2.6}$	$0.0^{+2.0}_{-0.0}$	$0.9^{+1.9}_{-0.4}$
129	–	$0.2^{+2.4}_{-0.0}$	$0.0^{+0.8}_{-0.0}$	$0.9^{+1.7}_{-0.0}$	$0.0^{+1.3}_{-0.0}$
137	–	$40.7^{+10.3}_{-12.0}$	$0.8^{+6.0}_{-0.0}$	$0.9^{+2.9}_{-0.0}$	$0.0^{+2.3}_{-0.0}$
142	M4	$0.7^{+6.3}_{-0.0}$	$0.5^{+2.4}_{-0.0}$	$2.6^{+2.3}_{-1.1}$	$1.3^{+2.9}_{-0.2}$
144	–	$0.0^{+5.3}_{-0.0}$	$0.0^{+2.1}_{-0.0}$	$6.1^{+1.6}_{-1.3}$	$4.4^{+2.6}_{-1.9}$
...		$23.3^{+91.2}_{-9.5}$	$22.1^{+33.3}_{-11.6}$	$10.9^{+26.9}_{-9.9}$	$0.0^{+41.9}_{-0.0}$
146	M4	$6.8^{+2.7}_{-1.1}$	$0.0^{+0.6}_{-0.0}$	$4.4^{+1.2}_{-1.6}$	$2.2^{+1.1}_{-1.1}$
...		$17.2^{+6.3}_{-2.6}$	$0.0^{+4.2}_{-0.0}$	$0.0^{+3.8}_{-0.0}$	$0.0^{+4.7}_{-0.0}$
147	–	$0.0^{+4.5}_{-0.0}$	$0.0^{+2.9}_{-0.0}$	$3.3^{+2.8}_{-1.3}$	$1.3^{+1.6}_{-0.9}$
148	K7	$7.4^{+15.4}_{-0.0}$	$2.5^{+2.7}_{-1.3}$	$3.5^{+3.4}_{-0.8}$	$0.0^{+1.0}_{-0.0}$
...		$3.8^{+36.6}_{-0.0}$	$17.8^{+16.9}_{-8.3}$	$30.8^{+24.5}_{-11.4}$	$1.9^{+10.7}_{-0.0}$
149	M0	$37.8^{+22.2}_{-13.3}$	$0.7^{+2.9}_{-0.0}$	$1.4^{+2.8}_{-0.9}$	$0.0^{+1.6}_{-0.0}$
...		$41.7^{+24.7}_{-28.1}$	$0.0^{+5.5}_{-0.0}$	$4.1^{+10.3}_{-1.5}$	$4.4^{+8.6}_{-3.6}$
Taurus					
04108+2910	M0	$0.1^{+0.4}_{-0.0}$	$0.5^{+1.4}_{-0.0}$	$2.9^{+1.2}_{-1.0}$	$0.0^{+0.8}_{-0.0}$
...		$13.2^{+9.3}_{-5.6}$	$0.1^{+6.5}_{-0.0}$	$4.0^{+10.8}_{-0.0}$	$0.0^{+9.9}_{-0.0}$
04200+2759	–	$4.7^{+1.5}_{-2.4}$	$0.1^{+2.2}_{-0.0}$	$0.4^{+1.2}_{-0.0}$	$0.0^{+0.9}_{-0.0}$
...		$14.3^{+11.5}_{-7.3}$	$1.2^{+4.5}_{-7.9}$	$4.2^{+5.1}_{-3.6}$	$3.8^{+8.2}_{-7.2}$
04216+2603	M1	$43.9^{+15.3}_{-22.8}$	$1.8^{+5.4}_{-0.7}$	$2.1^{+3.0}_{-1.0}$	$0.0^{+2.2}_{-0.0}$
...		$18.6^{+27.5}_{-9.0}$	$0.1^{+16.8}_{-0.0}$	$13.2^{+31.5}_{-10.7}$	$1.8^{+40.3}_{-8.2}$
04303+2240	–	$2.4^{+9.1}_{-0.0}$	$0.0^{+1.7}_{-0.0}$	$2.7^{+3.6}_{-0.0}$	$0.0^{+0.7}_{-0.0}$

ID	SpT	Oli/Pyr[a] % (0.1 μm)	Ens % (0.1 μm)	For % (0.1 μm)	Sil % (0.1 μm)
04370+2559	–	$3.1^{+7.3}_{-0.0}$	$1.2^{+2.3}_{-0.0}$	$0.7^{+1.5}_{-0.0}$	$0.0^{+0.4}_{-0.0}$
04385+2550	M0	$16.2^{+2.3}_{-7.9}$	$0.8^{+1.3}_{-0.5}$	$1.0^{+1.9}_{-0.0}$	$0.0^{+0.7}_{-0.0}$
$\cdots$		$13.2^{+11.7}_{-0.0}$	$0.0^{+2.2}_{-0.0}$	$1.6^{+3.3}_{-0.0}$	$5.7^{+11.4}_{-0.0}$
AATau	K7	$12.5^{+10.1}_{-0.6}$	$0.4^{+1.0}_{-0.0}$	$1.4^{+1.4}_{-0.7}$	$0.0^{+0.7}_{-0.0}$
$\cdots$		$2.6^{+19.7}_{-0.0}$	$19.2^{+15.3}_{-0.0}$	$0.0^{+24.2}_{-0.0}$	$18.3^{+22.4}_{-0.0}$
BPTau	K7	$29.9^{+5.4}_{-7.9}$	$1.1^{+0.9}_{-0.6}$	$1.0^{+1.3}_{-0.0}$	$0.0^{+0.3}_{-0.0}$
CITau	K7	$2.3^{+5.6}_{-0.0}$	$0.0^{+0.3}_{-0.0}$	$2.1^{+1.0}_{-0.0}$	$0.0^{+0.9}_{-0.0}$
$\cdots$		$14.8^{+12.4}_{-7.1}$	$0.3^{+1.5}_{-0.0}$	$3.5^{+10.3}_{-0.0}$	$7.5^{+9.9}_{-0.0}$
CWTau	K3	$8.2^{+1.9}_{-2.3}$	$1.0^{+0.7}_{-0.0}$	$1.0^{+1.5}_{-0.0}$	$0.2^{+2.4}_{-0.0}$
CoKuTau3	M1	$3.3^{+6.8}_{-0.5}$	$0.0^{+1.0}_{-0.0}$	$2.7^{+1.6}_{-1.4}$	$0.0^{+0.3}_{-0.0}$
$\cdots$		$15.2^{+9.6}_{-6.0}$	$5.3^{+10.2}_{-0.0}$	$3.8^{+1.9}_{-2.7}$	$0.2^{+4.6}_{-0.0}$
CoKuTau4	M1.5	$24.5^{+3.5}_{-17.1}$	$0.0^{+2.7}_{-0.0}$	$1.0^{+2.2}_{-0.0}$	$0.0^{+1.0}_{-0.0}$
$\cdots$		$13.4^{+8.4}_{-5.4}$	$0.3^{+1.3}_{-0.6}$	$0.0^{+1.4}_{-0.7}$	$13.5^{+9.1}_{-6.3}$
DDTau	M3	$10.6^{+4.7}_{-2.7}$	$2.6^{+3.8}_{-0.0}$	$2.5^{+2.6}_{-0.0}$	$0.0^{+1.4}_{-0.0}$
$\cdots$		$38.7^{+26.0}_{-23.6}$	$9.0^{+8.8}_{-6.1}$	$18.5^{+11.9}_{-8.6}$	$0.0^{+5.5}_{-0.0}$
DETau	M1	$11.0^{+6.9}_{-2.4}$	$0.4^{+1.7}_{-0.0}$	$3.3^{+2.5}_{-0.0}$	$0.0^{+0.6}_{-0.0}$
$\cdots$		$51.2^{+22.1}_{-24.7}$	$0.3^{+6.2}_{-0.0}$	$4.4^{+6.9}_{-0.0}$	$0.7^{+10.2}_{-0.0}$
DFTau	M0.5	$0.6^{+8.0}_{-0.0}$	$0.2^{+2.3}_{-0.0}$	$1.8^{+2.1}_{-0.0}$	$0.3^{+3.1}_{-0.0}$
DHTau	M2	$2.3^{+2.1}_{-0.3}$	$1.8^{+1.8}_{-0.8}$	$5.4^{+2.4}_{-1.2}$	$1.5^{+1.6}_{-0.9}$
$\cdots$		$32.0^{+16.2}_{-12.3}$	$2.5^{+6.0}_{-1.7}$	$3.4^{+8.5}_{-3.1}$	$0.0^{+5.6}_{-1.3}$
DKTau	M0	$13.0^{+3.8}_{-3.1}$	$0.6^{+0.9}_{-0.0}$	$1.9^{+1.3}_{-1.2}$	$3.3^{+1.3}_{-0.9}$
DLTau	K7	$0.1^{+5.6}_{-1.5}$	$0.0^{+1.1}_{-0.0}$	$3.0^{+2.3}_{-1.2}$	$5.0^{+3.5}_{-2.2}$
DMTau	M1	$4.1^{+13.6}_{-0.0}$	$0.0^{+1.8}_{-0.0}$	$4.7^{+2.3}_{-1.0}$	$0.0^{+1.2}_{-0.0}$
$\cdots$		$42.6^{+28.1}_{-17.1}$	$0.7^{+8.9}_{-0.0}$	$1.2^{+3.6}_{-0.0}$	$5.3^{+12.2}_{-4.8}$
DNTau	M0	$3.4^{+5.1}_{-0.0}$	$0.0^{+0.6}_{-0.0}$	$2.2^{+1.4}_{-0.6}$	$1.4^{+1.1}_{-0.9}$
$\cdots$		$33.7^{+39.1}_{-0.0}$	$0.2^{+9.1}_{-0.0}$	$0.0^{+18.1}_{-0.0}$	$0.0^{+7.6}_{-0.0}$
DOTau	M0	$1.2^{+8.4}_{-0.0}$	$0.0^{+3.8}_{-0.0}$	$1.6^{+2.7}_{-0.0}$	$0.3^{+4.0}_{-0.0}$
DPTau	M0.5	$35.1^{+13.7}_{-15.8}$	$0.0^{+1.5}_{-0.0}$	$1.1^{+1.9}_{-0.0}$	$0.0^{+1.6}_{-0.0}$
$\cdots$		$20.1^{+8.9}_{-8.0}$	$9.8^{+4.6}_{-5.1}$	$3.0^{+3.7}_{-2.1}$	$7.7^{+3.8}_{-3.8}$
DQTau	M0	$1.8^{+1.2}_{-1.3}$	$5.5^{+1.7}_{-1.4}$	$2.0^{+1.1}_{-0.7}$	$0.0^{+0.6}_{-0.0}$
$\cdots$		$14.4^{+12.0}_{-5.6}$	$0.1^{+8.7}_{-0.0}$	$0.0^{+8.0}_{-0.0}$	$0.0^{+3.3}_{-0.0}$
DRTau	K7	$25.0^{+5.8}_{-5.3}$	$0.0^{+0.7}_{-0.0}$	$1.0^{+1.5}_{-0.0}$	$0.0^{+0.6}_{-0.0}$
DSTau	K5	$35.9^{+7.1}_{-6.3}$	$0.8^{+2.9}_{-0.7}$	$2.8^{+2.3}_{-1.7}$	$0.2^{+1.2}_{-0.0}$
$\cdots$		$22.0^{+14.7}_{-10.3}$	$0.2^{+3.5}_{-1.8}$	$2.7^{+3.3}_{-1.8}$	$17.2^{+14.0}_{-9.7}$
F04147+2822	M4	$10.2^{+6.3}_{-0.0}$	$0.0^{+4.3}_{-0.0}$	$2.9^{+2.5}_{-0.0}$	$0.0^{+1.4}_{-0.0}$
F04192+2647	–	$3.4^{+12.4}_{-0.0}$	$0.1^{+0.8}_{-0.0}$	$3.6^{+1.7}_{-0.8}$	$0.0^{+0.7}_{-0.0}$
$\cdots$		$19.7^{+16.8}_{-7.4}$	$0.0^{+9.0}_{-1.6}$	$14.2^{+15.3}_{-7.1}$	$3.7^{+9.4}_{-4.5}$
F04262+2654	–	$0.0^{+1.0}_{-0.0}$	$2.1^{+2.0}_{-0.9}$	$0.0^{+1.2}_{-0.0}$	$3.9^{+2.8}_{-2.4}$
F04297+2246	–	$5.7^{+3.7}_{-1.3}$	$0.0^{+1.5}_{-0.0}$	$2.6^{+2.0}_{-1.5}$	$0.3^{+1.6}_{-0.0}$
$\cdots$		$24.7^{+61.7}_{-6.4}$	$3.5^{+15.1}_{-0.0}$	$0.1^{+32.3}_{-0.0}$	$0.0^{+17.6}_{-0.0}$
F04297+2246A	–	$6.0^{+4.4}_{-1.5}$	$3.6^{+1.8}_{-1.8}$	$3.1^{+1.0}_{-0.7}$	$0.0^{+0.9}_{-0.0}$

ID	SpT	Oli/Pyr[a] % (0.1 μm)	Ens % (0.1 μm)	For % (0.1 μm)	Sil % (0.1 μm)
...		$31.3^{+15.2}_{-10.4}$	$1.4^{+2.8}_{-0.0}$	$2.1^{+2.1}_{-0.0}$	$0.0^{+8.2}_{-0.0}$
F04570+2520	–	$2.9^{+11.6}_{-0.0}$	$0.1^{+1.7}_{-0.0}$	$0.1^{+3.9}_{-0.0}$	$0.0^{+2.9}_{-0.0}$
...		$0.1^{+4.1}_{-8.8}$	$0.0^{+1.8}_{-1.9}$	$0.0^{+9.0}_{-0.0}$	$40.0^{+8.3}_{-30.3}$
FMTau	M0	$56.0^{+14.4}_{-10.3}$	$0.0^{+2.4}_{-1.5}$	$2.1^{+2.6}_{-1.5}$	$0.0^{+1.7}_{-0.0}$
...		$25.0^{+46.8}_{-0.0}$	$2.4^{+23.7}_{-0.0}$	$3.5^{+4.5}_{-0.0}$	$1.2^{+17.8}_{-0.0}$
FNTau	M5	$11.3^{+3.5}_{-2.0}$	$4.5^{+2.7}_{-1.4}$	$2.7^{+2.0}_{-1.0}$	$0.1^{+2.0}_{-0.2}$
...		$10.6^{+52.1}_{-0.0}$	$9.3^{+29.6}_{-0.0}$	$12.6^{+37.1}_{-0.0}$	$0.0^{+22.9}_{-0.0}$
FOTau	M2	$12.4^{+6.8}_{-6.2}$	$0.0^{+4.2}_{-0.0}$	$2.5^{+6.5}_{-0.0}$	$0.2^{+3.3}_{-0.0}$
FPTau	M4	$25.8^{+9.3}_{-5.8}$	$3.7^{+2.6}_{-2.4}$	$0.9^{+1.6}_{-0.4}$	$0.0^{+2.4}_{-0.0}$
...		$8.6^{+8.4}_{-2.5}$	$7.2^{+6.1}_{-3.7}$	$2.4^{+2.7}_{-1.7}$	$10.1^{+6.6}_{-0.0}$
FQTau	M2	$17.9^{+15.3}_{-11.8}$	$1.0^{+7.1}_{-0.3}$	$0.4^{+3.3}_{-0.2}$	$5.2^{+7.0}_{-2.7}$
FSTau	M1	$32.5^{+10.9}_{-9.6}$	$1.6^{+3.0}_{-0.6}$	$0.3^{+1.4}_{-0.0}$	$1.3^{+1.7}_{-0.6}$
FTTau	c	$20.1^{+5.5}_{-3.9}$	$1.0^{+1.4}_{-0.8}$	$2.9^{+1.8}_{-1.5}$	$0.0^{+1.0}_{-0.0}$
...		$14.4^{+17.8}_{-0.0}$	$0.0^{+10.9}_{-0.0}$	$0.0^{+4.4}_{-0.0}$	$2.9^{+13.7}_{-0.0}$
FVTau	K5	$1.4^{+6.5}_{-0.0}$	$0.0^{+4.8}_{-0.0}$	$3.9^{+3.0}_{-0.0}$	$0.0^{+0.8}_{-0.0}$
FXTau	M1	$28.2^{+8.6}_{-5.6}$	$3.7^{+5.0}_{-0.0}$	$3.4^{+1.8}_{-1.6}$	$0.0^{+0.8}_{-0.0}$
...		$21.1^{+14.8}_{-3.5}$	$0.0^{+8.8}_{-0.0}$	$3.9^{+8.7}_{-0.0}$	$4.6^{+16.3}_{-0.0}$
FZTau	M0	$24.8^{+7.5}_{-10.9}$	$1.3^{+2.2}_{-0.0}$	$1.9^{+1.0}_{-0.9}$	$10.7^{+2.6}_{-2.6}$
GGTau	M0	$9.2^{+3.4}_{-3.7}$	$0.9^{+2.0}_{-0.0}$	$1.6^{+1.4}_{-0.0}$	$0.0^{+0.9}_{-0.0}$
GHTau	M2	$10.6^{+3.1}_{-3.9}$	$1.7^{+1.7}_{-0.9}$	$2.1^{+1.1}_{-1.3}$	$0.7^{+1.4}_{-0.7}$
...		$8.7^{+4.5}_{-4.5}$	$2.0^{+4.1}_{-2.4}$	$4.9^{+5.4}_{-4.4}$	$2.7^{+2.7}_{-2.3}$
GITau	K6	$35.6^{+10.0}_{-10.5}$	$0.4^{+3.0}_{-0.0}$	$1.4^{+1.3}_{-0.9}$	$0.0^{+0.6}_{-0.0}$
...		$16.0^{+10.5}_{-7.3}$	$8.4^{+5.7}_{-3.8}$	$11.1^{+6.0}_{-5.2}$	$1.9^{+5.1}_{-1.9}$
GKTau	K7	$64.5^{+7.3}_{-10.7}$	$0.0^{+0.9}_{-0.0}$	$3.1^{+1.5}_{-1.3}$	$0.0^{+0.7}_{-0.0}$
GMAur	K3	$37.3^{+9.4}_{-11.2}$	$0.0^{+3.2}_{-0.0}$	$3.1^{+2.8}_{-0.0}$	$0.0^{+1.3}_{-0.0}$
...		$15.7^{+29.0}_{-0.0}$	$0.7^{+5.5}_{-0.0}$	$0.4^{+29.4}_{-0.0}$	$17.3^{+33.6}_{-0.0}$
GOTau	M0	$12.0^{+6.5}_{-7.6}$	$0.0^{+4.8}_{-0.0}$	$3.4^{+2.8}_{-2.3}$	$0.1^{+2.0}_{-0.0}$
HKTau	M1	$1.0^{+2.9}_{-0.3}$	$0.4^{+2.0}_{-0.0}$	$1.8^{+1.3}_{-0.0}$	$0.1^{+1.1}_{-0.0}$
...		$19.5^{+29.6}_{-3.4}$	$5.3^{+10.3}_{-0.0}$	$1.3^{+8.8}_{-0.0}$	$11.1^{+54.3}_{-2.5}$
HNTau	K5	$13.9^{+6.7}_{-3.7}$	$0.0^{+0.4}_{-0.0}$	$0.8^{+0.7}_{-0.0}$	$0.0^{+0.4}_{-0.0}$
HOTau	M0.5	$10.8^{+3.7}_{-1.6}$	$0.7^{+1.0}_{-0.4}$	$2.0^{+2.6}_{-0.6}$	$0.0^{+0.7}_{-0.0}$
...		$38.3^{+19.0}_{-16.0}$	$0.0^{+1.2}_{-0.0}$	$1.6^{+4.0}_{-0.0}$	$0.0^{+2.7}_{-0.0}$
HPTau	K3	$57.4^{+10.9}_{-10.6}$	$0.0^{+0.8}_{-0.0}$	$1.0^{+1.0}_{-0.0}$	$0.0^{+0.9}_{-0.0}$
Haro6-37	K7	$11.4^{+13.5}_{-7.7}$	$0.0^{+1.6}_{-0.0}$	$3.4^{+2.2}_{-1.8}$	$3.0^{+2.9}_{-1.8}$
IPTau	M0	$28.0^{+9.2}_{-7.4}$	$0.8^{+2.4}_{-0.3}$	$2.5^{+1.4}_{-1.7}$	$0.0^{+0.5}_{-0.0}$
...		$17.0^{+8.1}_{-6.0}$	$0.2^{+7.4}_{-0.0}$	$1.7^{+5.7}_{-0.1}$	$8.2^{+5.6}_{-2.9}$
IQTau	M0.5	$17.3^{+4.1}_{-4.0}$	$0.0^{+1.4}_{-0.0}$	$2.0^{+1.7}_{-1.1}$	$0.0^{+0.9}_{-0.0}$
...		$24.3^{+8.9}_{-6.3}$	$0.0^{+1.2}_{-0.0}$	$0.7^{+2.7}_{-0.4}$	$1.6^{+3.1}_{-1.0}$
ISTau	K7	$0.0^{+4.1}_{-0.0}$	$0.0^{+3.3}_{-0.0}$	$6.8^{+2.9}_{-1.8}$	$11.6^{+3.8}_{-3.3}$
...		$3.0^{+24.8}_{-0.0}$	$0.0^{+31.7}_{-0.0}$	$10.4^{+55.5}_{-0.0}$	$6.8^{+66.0}_{-0.0}$
LkCa15	K5	$55.9^{+11.0}_{-15.1}$	$0.0^{+2.0}_{-0.0}$	$2.7^{+3.8}_{-0.0}$	$0.0^{+0.6}_{-0.0}$

ID	SpT	Oli/Pyr[a] % (0.1 μm)	Ens % (0.1 μm)	For % (0.1 μm)	Sil % (0.1 μm)
. . .		$22.0^{+11.7}_{-8.4}$	$9.2^{+6.1}_{-6.1}$	$0.0^{+2.0}_{-0.0}$	$10.2^{+7.4}_{-5.8}$
RWAur	K3	$26.1^{+9.0}_{-9.6}$	$0.3^{+1.0}_{-0.0}$	$1.5^{+2.1}_{-0.0}$	$0.0^{+0.5}_{-0.0}$
RYTau	G1	$6.5^{+3.8}_{-1.8}$	$8.4^{+1.7}_{-2.7}$	$1.1^{+0.8}_{-0.6}$	$8.0^{+1.7}_{-1.5}$
SUAur	G1	$20.2^{+5.0}_{-5.4}$	$0.0^{+0.6}_{-0.0}$	$1.3^{+1.0}_{-0.9}$	$0.0^{+0.6}_{-0.0}$
UYAur	K7	$19.9^{+6.4}_{-6.8}$	$0.1^{+2.6}_{-0.0}$	$0.0^{+1.3}_{-0.0}$	$0.0^{+1.9}_{-0.0}$
V710Tau	M1	$27.7^{+14.5}_{-19.2}$	$0.0^{+1.6}_{-0.0}$	$2.8^{+2.6}_{-1.8}$	$0.9^{+1.45}_{-0.6}$
V773Tau	K3	$26.2^{+24.6}_{-5.4}$	$3.8^{+5.9}_{-0.0}$	$1.3^{+2.3}_{-0.0}$	$0.0^{+1.8}_{-0.0}$
V836Tau	K7	$1.2^{+3.4}_{-0.0}$	$0.9^{+0.8}_{-0.6}$	$4.5^{+1.9}_{-0.8}$	$0.0^{+0.9}_{-0.0}$
. . .		$30.7^{+48.4}_{-8.9}$	$0.0^{+26.6}_{-0.0}$	$1.7^{+9.2}_{-0.0}$	$10.4^{+61.5}_{-0.0}$
V955Tau	K5	$0.0^{+1.3}_{-0.0}$	$0.0^{+0.9}_{-0.0}$	$6.3^{+2.5}_{-1.6}$	$10.7^{+3.1}_{-2.8}$
VYTau	M0	$2.5^{+13.5}_{-0.0}$	$0.0^{+12.4}_{-0.0}$	$3.3^{+16.1}_{-0.0}$	$0.0^{+8.4}_{-0.0}$
ZZTauIRS	M4.5	$16.0^{+6.3}_{-3.5}$	$0.7^{+3.0}_{-0.0}$	$0.7^{+2.2}_{-0.0}$	$0.1^{+1.2}_{-0.0}$
. . .		$16.1^{+8.6}_{-6.5}$	$0.0^{+2.0}_{-0.2}$	$8.1^{+6.9}_{-5.0}$	$6.0^{+4.7}_{-3.3}$
Upper Scorpius					
PBB2002 J160357.9	M2	$8.2^{+16.3}_{-2.1}$	$0.0^{+1.5}_{-0.0}$	$2.1^{+4.6}_{-0.2}$	$0.0^{+1.0}_{-0.0}$
PBB2002 J160823.2	K9	$2.4^{+6.2}_{-0.0}$	$0.0^{+5.3}_{-0.0}$	$3.8^{+6.2}_{-0.0}$	$0.0^{+1.1}_{-0.0}$
PBB2002 J160900.7	K9	$17.2^{+6.5}_{-4.5}$	$0.5^{+1.4}_{-0.0}$	$3.0^{+2.0}_{-1.6}$	$0.0^{+0.3}_{-0.0}$
PBB2002 J160959.4	M4	$17.7^{+31.6}_{-11.4}$	$0.0^{+2.7}_{-0.0}$	$4.8^{+3.8}_{-2.4}$	$0.5^{+2.5}_{-0.0}$
PBB2002 J161115.3	M1	$20.3^{+4.2}_{-12.7}$	$0.0^{+2.4}_{-0.0}$	$1.9^{+2.5}_{-1.4}$	$0.0^{+0.7}_{-0.0}$
PBB2002 J161420.2	M0	$6.5^{+1.4}_{-1.4}$	$0.0^{+0.5}_{-0.0}$	$1.4^{+0.9}_{-0.9}$	$0.0^{+0.3}_{-0.0}$
PZ99 J160357.6	K5	$0.0^{+3.1}_{-0.0}$	$0.0^{+2.8}_{-0.0}$	$2.8^{+5.1}_{-0.0}$	$0.0^{+3.2}_{-0.0}$
PZ99 J161411.0	K0	$0.0^{+2.0}_{-0.0}$	$0.0^{+4.0}_{-0.0}$	$1.1^{+2.1}_{-0.0}$	$1.4^{+4.4}_{-0.0}$
ScoPMS31	M0.5	$9.6^{+7.5}_{-11.3}$	$0.0^{+2.5}_{-0.0}$	$1.9^{+3.3}_{-1.8}$	$3.0^{+4.6}_{-1.6}$
η **Chamaeleontis**					
J0843	M3.4	$27.2^{+16.9}_{-11.0}$	$1.1^{+8.3}_{-0.0}$	$4.4^{+3.3}_{-0.0}$	$1.5^{+2.8}_{-0.0}$
RECX-5	M3.8	$36.1^{+23.4}_{-19.4}$	$0.0^{+2.9}_{-0.0}$	$12.3^{+8.7}_{-0.0}$	$0.3^{+14.8}_{-0.0}$
RECX-9	M4.4	$42.9^{+21.6}_{-34.1}$	$0.0^{+6.0}_{-0.0}$	$1.9^{+3.9}_{-1.0}$	$8.6^{+8.3}_{-6.7}$
RECX-11	K6.5	$36.9^{+18.1}_{-17.2}$	$1.4^{+3.4}_{-0.0}$	$3.4^{+8.4}_{-0.0}$	$2.6^{+4.2}_{-0.0}$

Table A.1 – Small dust composition derived using the "B2C" procedure.[b]

[a] Amorphous olivine and pyroxene combined.

[b] For each object, the first line corresponds to the warm component abundances, while the second line corresponds to the cold component abundances, when available.

ID	Oli/Pyr[a] % (1.5 μm)	Ens % (1.5 μm)	For % (1.5 μm)	Sil % (1.5 μm)	Oli/Pyr[a] % (6.0 μm)	Sil % (6.0 μm)
Serpens						
1	$53.7^{+16.5}_{-23.0}$	$3.5^{+3.5}_{-2.4}$	$0.0^{+2.9}_{-0.0}$	$1.0^{+2.1}_{-0.0}$	$7.8^{+3.8}_{-0.0}$	$0.6^{+1.9}_{-0.0}$
...	$29.3^{+6.2}_{-15.3}$	$6.8^{+4.3}_{-2.8}$	$0.2^{+1.1}_{-0.0}$	$0.3^{+1.4}_{-0.0}$	$9.7^{+4.7}_{-4.4}$	$5.5^{+1.4}_{-1.6}$
3	$43.9^{+19.8}_{-18.6}$	$0.2^{+4.1}_{-0.2}$	$2.7^{+3.8}_{-2.1}$	$0.0^{+2.9}_{-0.0}$	$15.7^{+3.2}_{-2.8}$	$0.0^{+1.0}_{-0.0}$
...	$32.9^{+34.1}_{-9.9}$	$4.9^{+19.2}_{-5.5}$	$0.0^{+13.9}_{-2.9}$	$12.7^{+22.5}_{-5.6}$	$10.2^{+7.4}_{-4.7}$	$1.8^{+2.2}_{-0.6}$
6	$38.2^{+11.6}_{-7.4}$	$1.0^{+1.4}_{-0.0}$	$1.0^{+1.4}_{-0.0}$	$0.0^{+1.4}_{-0.0}$	$28.8^{+4.5}_{-5.0}$	$4.8^{+3.6}_{-1.8}$
...	$46.1^{+19.8}_{-20.3}$	$4.7^{+6.2}_{-0.0}$	$1.2^{+2.3}_{-0.0}$	$2.7^{+4.4}_{-0.0}$	$25.4^{+8.6}_{-7.6}$	$3.7^{+2.2}_{-0.0}$
7	$75.6^{+26.0}_{-23.9}$	$0.0^{+5.6}_{-0.1}$	$3.7^{+4.7}_{-3.0}$	$0.0^{+5.1}_{-0.0}$	$0.0^{+9.8}_{-0.0}$	$16.1^{+4.4}_{-13.7}$
...	$6.0^{+7.7}_{-6.0}$	$14.1^{+8.8}_{-11.7}$	$0.0^{+3.0}_{-0.1}$	$24.7^{+14.3}_{-19.7}$	$25.6^{+14.0}_{-13.9}$	$0.0^{+3.5}_{-2.6}$
9	$27.4^{+5.7}_{-7.2}$	$3.8^{+2.4}_{-2.1}$	$2.5^{+1.5}_{-2.0}$	$0.0^{+1.3}_{-0.0}$	$3.6^{+4.1}_{-0.0}$	$3.7^{+1.7}_{-0.0}$
...	$9.4^{+6.7}_{-6.1}$	$0.0^{+3.8}_{-0.8}$	$0.0^{+1.5}_{-0.0}$	$7.5^{+5.8}_{-5.2}$	$24.4^{+16.2}_{-14.3}$	$2.7^{+7.2}_{-3.2}$
10	$37.6^{+17.3}_{-16.8}$	$7.2^{+4.2}_{-3.5}$	$5.3^{+6.6}_{-2.9}$	$0.2^{+4.0}_{-0.0}$	$31.6^{+18.5}_{-8.3}$	$9.5^{+7.6}_{-4.4}$
...	$39.0^{+23.6}_{-10.3}$	$0.0^{+20.1}_{-0.0}$	$3.3^{+9.6}_{-1.3}$	$0.0^{+9.3}_{-0.0}$	$14.8^{+35.1}_{-1.2}$	$3.6^{+14.1}_{-0.5}$
14	$54.7^{+31.3}_{-20.3}$	$4.8^{+20.8}_{-0.0}$	$0.0^{+4.9}_{-0.0}$	$0.0^{+8.7}_{-0.0}$	$13.5^{+9.3}_{-5.8}$	$12.8^{+10.4}_{-4.0}$
15	$51.3^{+9.3}_{-16.1}$	$3.0^{+3.4}_{-1.5}$	$0.0^{+1.6}_{-0.0}$	$0.8^{+1.8}_{-0.0}$	$1.2^{+2.2}_{-0.0}$	$5.0^{+2.0}_{-0.5}$
...	$34.9^{+9.9}_{-12.2}$	$0.0^{+1.0}_{-0.0}$	$5.4^{+2.0}_{-2.1}$	$0.0^{+2.1}_{-0.6}$	$14.6^{+4.7}_{-4.6}$	$3.0^{+1.4}_{-1.9}$
21	$20.2^{+10.1}_{-12.9}$	$0.1^{+4.2}_{-0.0}$	$19.2^{+11.1}_{-9.1}$	$0.0^{+4.2}_{-0.0}$	$43.3^{+6.5}_{-21.3}$	$12.3^{+8.6}_{-9.1}$
...	$42.5^{+22.6}_{-24.9}$	$2.7^{+14.8}_{-0.0}$	$0.5^{+3.8}_{-0.0}$	$0.0^{+14.2}_{-0.0}$	$9.6^{+8.7}_{-3.3}$	$8.7^{+5.2}_{-7.5}$
29	$71.0^{+26.0}_{-49.2}$	$0.0^{+9.3}_{-0.0}$	$4.4^{+9.4}_{-3.1}$	$0.0^{+7.9}_{-0.0}$	$13.0^{+6.4}_{-7.}$	$5.6^{+14.7}_{-3.1}$
30	$12.5^{+8.5}_{-6.4}$	$12.5^{+8.1}_{-3.4}$	$1.3^{+5.9}_{-0.8}$	$1.5^{+5.0}_{-0.8}$	$64.2^{+18.1}_{-47.0}$	$0.0^{+21.4}_{-0.0}$
...	$8.0^{+58.7}_{-19.4}$	$9.1^{+14.9}_{-5.1}$	$29.6^{+44.9}_{-24.3}$	$11.4^{+37.5}_{-10.3}$	$14.0^{+36.3}_{-10.3}$	$2.1^{+9.6}_{-2.3}$
31	$15.0^{+2.6}_{-1.5}$	$2.5^{+1.2}_{-0.0}$	$3.4^{+1.5}_{-0.0}$	$0.4^{+0.4}_{-0.0}$	$76.1^{+7.8}_{-5.4}$	$0.6^{+1.0}_{-0.0}$
...	$24.0^{+4.7}_{-4.0}$	$2.3^{+2.0}_{-0.0}$	$0.5^{+1.7}_{-0.0}$	$5.4^{+4.4}_{-2.6}$	$9.2^{+4.8}_{-5.2}$	$17.6^{+3.3}_{-4.7}$
36	$51.9^{+12.1}_{-12.3}$	$1.0^{+2.9}_{-0.6}$	$3.3^{+2.8}_{-2.5}$	$0.0^{+1.6}_{-0.0}$	$10.8^{+2.8}_{-2.6}$	$9.0^{+2.7}_{-4.8}$
...	$38.1^{+11.0}_{-14.3}$	$0.0^{+2.4}_{-0.0}$	$0.0^{+2.9}_{-0.0}$	$0.2^{+8.7}_{-0.0}$	$19.6^{+5.9}_{-7.7}$	$0.1^{+0.3}_{-1.4}$
40	$41.2^{+17.3}_{-25.0}$	$22.5^{+11.0}_{-8.8}$	$17.9^{+11.6}_{-7.4}$	$0.0^{+5.5}_{-0.0}$	$4.5^{+9.7}_{-0.2}$	$0.0^{+9.8}_{-0.0}$
...	$18.2^{+9.5}_{-13.8}$	$2.1^{+12.8}_{-1.9}$	$13.4^{+7.8}_{-9.8}$	$0.0^{+3.0}_{-0.0}$	$0.2^{+9.7}_{-0.0}$	$22.3^{+11.2}_{-12.6}$
41	$66.6^{+6.8}_{-58.2}$	$3.4^{+16.3}_{-0.0}$	$16.4^{+11.3}_{-8.6}$	$0.0^{+6.3}_{-0.0}$	$2.6^{+13.8}_{-0.0}$	$0.0^{+14.8}_{-0.0}$
43	$42.1^{+19.1}_{-27.0}$	$7.1^{+8.9}_{-5.1}$	$2.7^{+7.1}_{-2.0}$	$0.0^{+3.5}_{-0.0}$	$37.2^{+15.8}_{-19.3}$	$2.0^{+12.7}_{-0.0}$
48	$73.3^{+28.2}_{-35.2}$	$0.0^{+9.2}_{-0.0}$	$0.0^{+13.8}_{-0.1}$	$1.1^{+9.9}_{-0.7}$	$6.0^{+8.4}_{-2.1}$	$9.9^{+4.6}_{-6.9}$
...	$18.7^{+10.0}_{-17.6}$	$0.0^{+7.5}_{-0.1}$	$4.1^{+12.0}_{-3.5}$	$8.6^{+5.8}_{-8.1}$	$7.4^{+5.6}_{-4.7}$	$7.5^{+4.4}_{-6.6}$
53	$30.2^{+18.2}_{-14.6}$	$10.1^{+19.9}_{-5.8}$	$0.0^{+11.6}_{-0.0}$	$2.3^{+15.6}_{-0.7}$	$32.9^{+27.1}_{-6.7}$	$8.1^{+9.4}_{-5.3}$
55	$71.0^{+16.2}_{-26.2}$	$0.0^{+3.0}_{-0.0}$	$0.0^{+2.7}_{-0.0}$	$1.9^{+3.0}_{-0.0}$	$4.2^{+1.5}_{-0.8}$	$2.1^{+0.9}_{-0.7}$
...	$20.5^{+71.1}_{-20.0}$	$15.7^{+72.9}_{-9.9}$	$0.0^{+22.3}_{-0.1}$	$4.8^{+65.6}_{-4.2}$	$2.9^{+5.8}_{-1.6}$	$1.9^{+6.0}_{-1.8}$
56	$44.6^{+16.6}_{-28.5}$	$5.0^{+7.9}_{-2.7}$	$1.7^{+7.3}_{-0.5}$	$0.0^{+4.6}_{-0.0}$	$29.5^{+11.8}_{-11.8}$	$6.1^{+12.2}_{-0.1}$
...	$29.8^{+11.0}_{-12.0}$	$0.0^{+15.8}_{-0.0}$	$1.1^{+7.5}_{-0.0}$	$0.0^{+3.2}_{-0.0}$	$19.3^{+24.2}_{-7.9}$	$1.6^{+27.0}_{-0.0}$
57	$72.0^{+29.0}_{-40.9}$	$10.5^{+13.3}_{-6.6}$	$0.0^{+7.1}_{-0.0}$	$0.0^{+7.1}_{-0.0}$	$6.5^{+19.1}_{-0.0}$	$0.0^{+9.5}_{-0.0}$
...	$13.1^{+55.6}_{-4.8}$	$0.3^{+27.7}_{-0.0}$	$4.5^{+61.3}_{-0.0}$	$1.7^{+25.5}_{-4.5}$	$25.1^{+85.7}_{-3.7}$	$17.2^{+81.4}_{-5.0}$
58	$29.9^{+4.6}_{-6.7}$	$1.0^{+2.2}_{-0.7}$	$7.1^{+3.0}_{-2.1}$	$0.0^{+1.8}_{-0.0}$	$28.3^{+6.5}_{-11.5}$	$25.4^{+6.4}_{-8.7}$
...	$57.0^{+24.9}_{-36.3}$	$0.0^{+7.5}_{-0.0}$	$0.0^{+8.0}_{-0.0}$	$0.0^{+6.2}_{-0.0}$	$4.7^{+2.9}_{-1.4}$	$2.8^{+2.5}_{-0.0}$

ID	Oli/Pyr[a] % (1.5 μm)	Ens % (1.5 μm)	For % (1.5 μm)	Sil % (1.5 μm)	Oli/Pyr[a] % (6.0 μm)	Sil % (6.0 μm)
60	$41.7^{+31.4}_{-21.7}$	$8.5^{+13.1}_{-5.2}$	$3.3^{+14.0}_{-2.3}$	$0.0^{+13.7}_{-0.0}$	$4.9^{+14.8}_{-1.7}$	$26.5^{+17.0}_{-14.6}$
61	$52.1^{+11.9}_{-13.2}$	$3.1^{+5.1}_{-0.0}$	$6.2^{+3.6}_{-3.0}$	$0.0^{+2.4}_{-0.0}$	$11.3^{+4.2}_{-3.0}$	$13.3^{+1.8}_{-6.3}$
...	$38.7^{+6.6}_{-6.3}$	$0.0^{+1.6}_{-0.0}$	$1.1^{+0.9}_{-0.6}$	$1.2^{+2.3}_{-0.1}$	$7.5^{+5.7}_{-0.0}$	$12.7^{+6.0}_{-2.4}$
65	$21.3^{+9.9}_{-16.6}$	$8.6^{+5.3}_{-5.4}$	$8.3^{+4.2}_{-3.2}$	$0.0^{+1.3}_{-2.7}$	$41.8^{+15.0}_{-22.4}$	$13.9^{+7.9}_{-10.4}$
...	$6.2^{+9.7}_{-2.8}$	$0.3^{+9.6}_{-0.0}$	$0.0^{+4.0}_{-0.0}$	$2.7^{+3.8}_{-1.4}$	$8.5^{+28.2}_{-2.5}$	$18.4^{+20.9}_{-7.7}$
66	$46.5^{+15.4}_{-15.6}$	$0.8^{+5.1}_{-0.0}$	$2.9^{+5.0}_{-1.6}$	$0.0^{+2.3}_{-0.0}$	$38.2^{+18.7}_{-18.7}$	$8.7^{+8.2}_{-2.5}$
...	$26.3^{+25.8}_{-8.9}$	$1.7^{+11.2}_{-0.0}$	$0.4^{+8.1}_{-0.0}$	$3.2^{+19.6}_{-0.0}$	$11.0^{+21.0}_{-0.0}$	$15.7^{+6.8}_{-8.1}$
71	$24.2^{+24.6}_{-11.4}$	$3.0^{+20.1}_{-0.3}$	$4.7^{+25.9}_{-0.0}$	$1.9^{+12.1}_{-0.5}$	$56.6^{+55.6}_{-10.9}$	$0.0^{+10.4}_{-0.0}$
74	$0.0^{+6.3}_{-0.0}$	$5.8^{+3.4}_{-3.0}$	$16.1^{+5.7}_{-0.0}$	$0.0^{+4.7}_{-0.0}$	$58.3^{+17.9}_{-31.2}$	$0.0^{+18.2}_{-0.0}$
...	$24.2^{+26.5}_{-9.8}$	$1.8^{+23.4}_{-0.0}$	$5.4^{+31.1}_{-0.0}$	$0.0^{+12.8}_{-0.0}$	$9.9^{+22.5}_{-5.9}$	$7.8^{+23.4}_{-7.1}$
75	$15.0^{+>15.0}_{-0.0}$	$5.2^{+36.0}_{-0.0}$	$0.0^{+32.5}_{-0.0}$	$0.0^{+51.2}_{-0.0}$	$59.6^{+42.6}_{-33.4}$	$16.0^{+69.6}_{-0.0}$
76	$65.0^{+15.7}_{-29.6}$	$0.0^{+3.3}_{-0.0}$	$1.3^{+5.3}_{-0.0}$	$0.0^{+3.0}_{-0.0}$	$23.7^{+13.5}_{-3.9}$	$0.1^{+2.0}_{-0.0}$
...	$29.6^{+12.4}_{-12.1}$	$0.0^{+3.3}_{-0.0}$	$12.9^{+7.2}_{-5.2}$	$0.0^{+2.1}_{-0.0}$	$12.2^{+5.9}_{-4.3}$	$0.0^{+2.1}_{-1.0}$
80	$7.5^{+2.0}_{-0.0}$	$3.2^{+1.3}_{-1.5}$	$3.1^{+1.0}_{-0.9}$	$0.0^{+0.6}_{-0.0}$	$84.7^{+8.2}_{-6.6}$	$0.0^{+1.1}_{-0.0}$
...	$15.4^{+50.2}_{-0.0}$	$6.2^{+18.2}_{-0.0}$	$0.8^{+10.1}_{-0.0}$	$3.1^{+9.0}_{-0.0}$	$22.6^{+78.6}_{-0.0}$	$29.2^{+67.6}_{-0.0}$
81	$54.5^{+5.4}_{-3.7}$	$0.0^{+0.7}_{-0.0}$	$6.1^{+1.9}_{-2.0}$	$0.0^{+0.5}_{-0.0}$	$15.6^{+2.5}_{-2.7}$	$8.8^{+1.6}_{-1.2}$
...	$31.4^{+8.3}_{-4.4}$	$7.0^{+2.4}_{-2.2}$	$0.0^{+0.3}_{-0.0}$	$4.0^{+2.3}_{-2.0}$	$7.7^{+1.0}_{-1.2}$	$4.5^{+0.7}_{-0.9}$
86	$36.0^{+3.4}_{-3.0}$	$0.0^{+0.2}_{-0.0}$	$3.3^{+1.1}_{-1.7}$	$0.0^{+0.2}_{-0.0}$	$44.1^{+4.2}_{-4.4}$	$0.1^{+0.7}_{-0.0}$
...	$18.2^{+55.5}_{-0.0}$	$10.0^{+27.7}_{-0.0}$	$0.5^{+20.3}_{-0.0}$	$6.0^{+29.6}_{-0.0}$	$10.7^{+39.6}_{-0.0}$	$13.7^{+38.7}_{-0.0}$
88	$67.1^{+20.5}_{-17.3}$	$10.3^{+7.1}_{-5.0}$	$0.0^{+3.6}_{-0.0}$	$3.1^{+2.4}_{-2.0}$	$9.9^{+6.3}_{-1.8}$	$0.9^{+1.2}_{-0.6}$
...	$2.1^{+21.3}_{-6.5}$	$0.0^{+7.7}_{-0.0}$	$30.6^{+29.1}_{-12.4}$	$0.6^{+9.9}_{-3.0}$	$17.6^{+32.8}_{-10.1}$	$3.1^{+11.2}_{-3.5}$
89	$0.0^{+0.7}_{-0.0}$	$0.0^{+0.6}_{-0.0}$	$1.4^{+0.9}_{-0.0}$	$0.0^{+0.6}_{-0.0}$	$94.4^{+18.8}_{-75.4}$	$0.0^{+3.7}_{-0.0}$
90	$49.1^{+24.7}_{-30.7}$	$3.7^{+9.5}_{-1.8}$	$0.0^{+10.1}_{-1.8}$	$2.8^{+5.5}_{-1.9}$	$5.4^{+16.4}_{-1.2}$	$10.0^{+12.9}_{-1.8}$
...	$16.8^{+54.1}_{-0.0}$	$3.6^{+38.8}_{-0.0}$	$9.2^{+58.7}_{-0.0}$	$0.8^{+24.8}_{-0.0}$	$12.5^{+52.2}_{-0.0}$	$9.2^{+39.3}_{-0.0}$
92	$35.8^{+25.4}_{-8.5}$	$5.7^{+7.5}_{-2.1}$	$0.0^{+3.5}_{-0.0}$	$0.0^{+2.4}_{-0.0}$	$44.0^{+13.1}_{-15.9}$	$6.3^{+14.1}_{-2.4}$
...	$31.2^{+9.3}_{-15.1}$	$0.4^{+6.5}_{-0.0}$	$6.8^{+3.8}_{-3.9}$	$0.0^{+10.0}_{-0.0}$	$37.9^{+19.4}_{-12.3}$	$0.0^{+12.6}_{-0.0}$
96	$56.5^{+23.3}_{-35.1}$	$3.8^{+12.9}_{-1.8}$	$0.0^{+15.2}_{-0.0}$	$3.0^{+9.2}_{-0.8}$	$7.4^{+6.7}_{-4.3}$	$5.8^{+10.1}_{-1.5}$
100	$1.2^{+88.8}_{-0.0}$	$9.5^{+81.9}_{-0.0}$	$0.0^{+34.1}_{-0.0}$	$1.1^{+106.2}_{-0.0}$	$81.8^{+47.3}_{-54.1}$	$3.1^{+11.6}_{-4.1}$
101	$60.2^{+22.6}_{-33.4}$	$1.9^{+8.8}_{-0.0}$	$2.6^{+7.5}_{-0.5}$	$0.0^{+5.3}_{-0.0}$	$6.6^{+10.1}_{-0.0}$	$1.6^{+5.2}_{-0.0}$
...	$55.9^{+7.1}_{-11.9}$	$0.0^{+3.7}_{-0.0}$	$9.5^{+4.8}_{-6.1}$	$0.0^{+2.7}_{-0.0}$	$13.6^{+3.5}_{-7.2}$	$0.1^{+3.0}_{-0.0}$
103	$38.0^{+7.0}_{-5.0}$	$2.0^{+2.3}_{-1.2}$	$7.8^{+2.4}_{-2.1}$	$0.0^{+1.8}_{-0.0}$	$27.6^{+6.0}_{-5.5}$	$18.9^{+4.2}_{-4.1}$
...	$35.1^{+18.1}_{-20.5}$	$0.0^{+6.3}_{-0.0}$	$5.1^{+5.6}_{-0.0}$	$4.2^{+9.0}_{-0.0}$	$15.7^{+8.5}_{-4.5}$	$17.3^{+2.3}_{-17.7}$
104	$70.4^{+35.4}_{-48.8}$	$4.7^{+12.4}_{-3.6}$	$0.0^{+10.2}_{-0.0}$	$0.0^{+6.1}_{-0.0}$	$14.2^{+17.3}_{-6.1}$	$0.1^{+14.8}_{-0.0}$
106	$0.1^{+24.9}_{-0.0}$	$10.0^{+21.9}_{-5.5}$	$0.3^{+10.7}_{-0.0}$	$1.1^{+15.6}_{-0.0}$	$73.7^{+19.9}_{-61.5}$	$0.0^{+20.7}_{-0.0}$
113	$24.9^{+12.9}_{-10.3}$	$10.3^{+4.9}_{-3.4}$	$5.8^{+5.2}_{-2.2}$	$0.0^{+2.0}_{-0.0}$	$42.5^{+13.4}_{-17.9}$	$8.8^{+7.0}_{-4.4}$
...	$36.2^{+21.8}_{-13.5}$	$1.7^{+9.0}_{-0.0}$	$0.0^{+5.8}_{-0.0}$	$0.0^{+7.9}_{-0.0}$	$10.9^{+11.9}_{-1.3}$	$8.6^{+10.8}_{-4.2}$
114	$34.7^{+17.7}_{-12.5}$	$4.2^{+3.2}_{-2.8}$	$1.9^{+6.6}_{-0.6}$	$0.0^{+2.3}_{-0.0}$	$51.8^{+15.2}_{-17.1}$	$17.4^{+10.1}_{-5.2}$
115	$65.7^{+17.3}_{-48.2}$	$0.0^{+4.3}_{-0.0}$	$0.0^{+4.3}_{-0.0}$	$0.0^{+3.5}_{-0.0}$	$25.6^{+10.3}_{-14.5}$	$2.6^{+4.6}_{-0.9}$
117	$5.1^{+6.4}_{-0.2}$	$10.7^{+2.1}_{-3.2}$	$0.0^{+0.9}_{-0.0}$	$0.0^{+0.9}_{-0.0}$	$2.1^{+2.0}_{-0.0}$	$0.2^{+1.2}_{-0.0}$
...	$23.6^{+14.9}_{-6.8}$	$0.8^{+2.1}_{-0.4}$	$0.0^{+6.8}_{-0.0}$	$2.3^{+3.9}_{-2.4}$	$2.4^{+2.8}_{-1.3}$	$1.7^{+2.2}_{-0.9}$
119	$11.1^{+56.7}_{-2.7}$	$0.2^{+25.1}_{-0.0}$	$0.6^{+41.3}_{-0.0}$	$0.3^{+33.6}_{-0.0}$	$84.0^{+58.6}_{-26.7}$	$0.0^{+96.2}_{-0.0}$
122	$52.6^{+10.1}_{-35.4}$	$6.4^{+15.0}_{-3.1}$	$0.0^{+10.0}_{-0.0}$	$0.0^{+4.4}_{-0.0}$	$1.7^{+17.3}_{-1.0}$	$7.1^{+14.6}_{-1.1}$

ID	Oli/Pyr[a] % (1.5 μm)	Ens % (1.5 μm)	For % (1.5 μm)	Sil % (1.5 μm)	Oli/Pyr[a] % (6.0 μm)	Sil % (6.0 μm)
. . .	$27.8^{+39.9}_{-13.3}$	$0.9^{+11.2}_{-0.0}$	$0.0^{+14.3}_{-0.0}$	$0.0^{+10.5}_{-1.7}$	$11.8^{+13.6}_{-4.3}$	$5.7^{+18.0}_{-0.0}$
123	$41.2^{+11.7}_{-16.8}$	$4.1^{+6.4}_{-0.6}$	$0.0^{+4.2}_{-0.0}$	$2.7^{+3.7}_{-1.4}$	$4.0^{+6.8}_{-0.1}$	$0.0^{+0.5}_{-0.0}$
125	$56.9^{+11.9}_{-23.8}$	$0.0^{+5.0}_{-0.0}$	$0.0^{+7.2}_{-0.0}$	$0.0^{+4.4}_{-0.0}$	$30.8^{+6.4}_{-16.9}$	$5.0^{+11.2}_{-1.2}$
. . .	$29.1^{+9.2}_{-13.7}$	$7.0^{+4.1}_{-5.2}$	$0.2^{+1.8}_{-0.0}$	$0.0^{+3.8}_{-0.0}$	$16.0^{+6.1}_{-7.7}$	$5.1^{+3.2}_{-3.1}$
127	$0.0^{+2.0}_{-0.0}$	$0.0^{+3.1}_{-0.0}$	$1.5^{+5.7}_{-0.0}$	$1.3^{+4.4}_{-0.5}$	$91.5^{+71.4}_{-21.7}$	$0.0^{+7.8}_{-0.0}$
129	$14.7^{+7.3}_{-4.2}$	$1.7^{+4.2}_{-0.0}$	$0.0^{+2.3}_{-0.0}$	$0.0^{+0.9}_{-0.0}$	$82.5^{+20.0}_{-55.0}$	$0.0^{+6.7}_{-0.0}$
137	$39.0^{+10.8}_{-19.2}$	$5.6^{+3.4}_{-4.2}$	$5.8^{+4.1}_{-3.6}$	$0.0^{+3.2}_{-0.0}$	$0.0^{+2.3}_{-0.0}$	$7.1^{+4.7}_{-2.1}$
142	$58.7^{+20.7}_{-33.8}$	$4.0^{+6.6}_{-2.6}$	$1.9^{+7.4}_{-0.0}$	$4.5^{+4.9}_{-2.7}$	$25.7^{+9.0}_{-10.1}$	$0.1^{+6.1}_{-0.0}$
144	$46.2^{+6.0}_{-23.0}$	$11.2^{+4.4}_{-3.3}$	$0.0^{+3.0}_{-0.0}$	$0.0^{+3.0}_{-0.0}$	$32.0^{+13.9}_{-7.4}$	$0.0^{+2.6}_{-0.0}$
. . .	$7.3^{+21.8}_{-7.8}$	$10.5^{+20.1}_{-6.9}$	$12.1^{+10.9}_{-6.2}$	$0.0^{+22.2}_{-0.0}$	$8.3^{+19.9}_{-3.5}$	$5.5^{+14.3}_{-3.7}$
146	$34.1^{+4.5}_{-6.7}$	$0.0^{+1.1}_{-0.0}$	$4.1^{+3.0}_{-2.3}$	$0.0^{+1.3}_{-0.0}$	$32.6^{+8.3}_{-7.7}$	$15.6^{+2.9}_{-4.7}$
. . .	$27.7^{+8.1}_{-8.0}$	$0.0^{+3.8}_{-0.0}$	$2.2^{+1.5}_{-0.0}$	$0.0^{+2.6}_{-0.0}$	$52.9^{+19.8}_{-10.5}$	$0.0^{+8.7}_{-0.0}$
147	$34.1^{+18.9}_{-10.9}$	$9.8^{+9.0}_{-4.6}$	$0.0^{+3.5}_{-0.6}$	$0.7^{+4.8}_{-0.0}$	$50.7^{+18.1}_{-41.6}$	$0.0^{+15.4}_{-0.0}$
148	$70.6^{+18.2}_{-49.9}$	$3.7^{+8.0}_{-2.0}$	$0.0^{+5.3}_{-0.0}$	$2.5^{+5.1}_{-0.0}$	$5.1^{+8.9}_{-0.0}$	$4.6^{+5.1}_{-1.1}$
. . .	$2.0^{+13.4}_{-0.0}$	$10.9^{+16.2}_{-7.5}$	$5.0^{+17.7}_{-3.7}$	$2.9^{+21.5}_{-0.0}$	$24.7^{+18.4}_{-9.6}$	$0.1^{+4.7}_{-0.0}$
149	$24.1^{+10.8}_{-10.7}$	$3.9^{+5.5}_{-1.6}$	$0.0^{+2.3}_{-0.0}$	$1.3^{+2.6}_{-0.0}$	$30.1^{+11.2}_{-8.9}$	$0.4^{+8.8}_{-0.0}$
. . .	$28.3^{+14.5}_{-21.1}$	$3.7^{+13.2}_{-0.5}$	$1.1^{+12.7}_{-0.1}$	$0.0^{+8.3}_{-0.0}$	$8.8^{+6.5}_{-1.2}$	$7.8^{+5.4}_{-1.9}$
Taurus						
04108+2910	$10.4^{+4.1}_{-6.1}$	$11.2^{+3.1}_{-4.7}$	$3.6^{+3.1}_{-1.6}$	$0.0^{+0.9}_{-0.0}$	$71.3^{+16.2}_{-29.0}$	$0.0^{+8.4}_{-0.0}$
. . .	$58.5^{+22.3}_{-17.8}$	$0.0^{+8.0}_{-0.0}$	$0.0^{+7.8}_{-0.0}$	$0.0^{+45.4}_{-0.0}$	$12.9^{+15.9}_{-5.3}$	$11.4^{+7.1}_{-6.4}$
04200+2759	$48.4^{+14.7}_{-13.1}$	$7.9^{+6.2}_{-4.1}$	$2.8^{+5.3}_{-0.0}$	$0.0^{+2.5}_{-0.0}$	$19.6^{+9.4}_{-5.6}$	$16.0^{+7.1}_{-11.1}$
. . .	$58.6^{+32.2}_{-26.4}$	$0.0^{+9.8}_{-0.0}$	$0.0^{+18.6}_{-0.0}$	$7.2^{+31.8}_{-20.3}$	$10.3^{+7.3}_{-5.6}$	$0.4^{+2.6}_{-1.4}$
04216+2603	$18.9^{+17.6}_{-12.3}$	$6.4^{+1.7}_{-5.1}$	$0.0^{+2.5}_{-0.0}$	$0.0^{+2.8}_{-0.0}$	$27.1^{+9.7}_{-9.5}$	$0.0^{+9.3}_{-0.0}$
. . .	$4.4^{+16.5}_{-5.1}$	$2.1^{+18.1}_{-3.1}$	$1.5^{+20.5}_{-0.0}$	$10.5^{+17.2}_{-3.1}$	$44.5^{+31.4}_{-17.3}$	$3.2^{+13.5}_{-4.3}$
04303+2240	$74.2^{+25.2}_{-17.9}$	$3.5^{+8.5}_{-6.3}$	$9.6^{+10.7}_{-6.3}$	$2.0^{+4.0}_{-0.4}$	$0.0^{+1.0}_{-0.0}$	$5.5^{+9.8}_{-0.0}$
04370+2559	$80.2^{+16.5}_{-33.6}$	$0.3^{+7.0}_{-0.0}$	$1.2^{+5.7}_{-0.0}$	$0.0^{+2.1}_{-0.0}$	$4.9^{+5.3}_{-0.0}$	$8.3^{+2.8}_{-2.3}$
04385+2550	$55.1^{+12.3}_{-12.6}$	$4.8^{+4.9}_{-3.0}$	$3.7^{+3.8}_{-0.0}$	$0.0^{+2.5}_{-0.0}$	$6.4^{+1.9}_{-1.7}$	$11.9^{+2.7}_{-6.2}$
. . .	$47.7^{+34.5}_{-12.4}$	$0.0^{+16.4}_{-0.0}$	$0.0^{+9.1}_{-0.0}$	$19.9^{+39.6}_{-0.0}$	$8.1^{+5.0}_{-1.6}$	$3.9^{+6.0}_{-0.0}$
AATau	$30.6^{+7.5}_{-8.4}$	$3.4^{+2.6}_{-2.6}$	$2.6^{+3.3}_{-1.6}$	$2.1^{+2.6}_{-0.0}$	$45.7^{+13.6}_{-20.6}$	$1.3^{+5.3}_{-0.6}$
. . .	$9.3^{+20.9}_{-0.0}$	$8.3^{+16.8}_{-0.0}$	$4.5^{+6.0}_{-0.0}$	$7.0^{+13.7}_{-0.0}$	$29.6^{+37.2}_{-0.0}$	$1.2^{+24.4}_{-0.0}$
BPTau	$25.4^{+5.6}_{-8.4}$	$0.8^{+1.1}_{-0.0}$	$0.0^{+0.8}_{-0.0}$	$0.0^{+0.5}_{-0.0}$	$31.6^{+6.8}_{-10.3}$	$10.3^{+2.9}_{-4.1}$
CITau	$51.8^{+10.5}_{-12.3}$	$4.6^{+6.6}_{-1.0}$	$2.8^{+3.7}_{-1.3}$	$0.1^{+1.5}_{-0.0}$	$17.8^{+13.8}_{-7.8}$	$18.7^{+5.1}_{-3.9}$
. . .	$14.5^{+12.3}_{-4.3}$	$1.9^{+19.1}_{-0.0}$	$0.0^{+3.4}_{-0.0}$	$9.7^{+7.2}_{-5.8}$	$27.4^{+11.9}_{-11.2}$	$20.3^{+36.9}_{-6.0}$
CWTau	$23.5^{+10.5}_{-5.3}$	$1.2^{+3.5}_{-0.0}$	$0.0^{+1.1}_{-0.0}$	$0.0^{+0.8}_{-0.0}$	$46.4^{+9.9}_{-19.3}$	$18.5^{+7.4}_{-4.7}$
CoKuTau3	$63.5^{+15.4}_{-24.8}$	$3.7^{+4.5}_{-2.0}$	$0.4^{+3.2}_{-0.0}$	$0.0^{+2.0}_{-0.0}$	$26.0^{+8.3}_{-4.4}$	$0.3^{+4.4}_{-0.0}$
. . .	$24.1^{+10.5}_{-8.6}$	$1.8^{+3.0}_{-0.0}$	$14.3^{+25.3}_{-4.3}$	$4.4^{+7.3}_{-2.8}$	$22.5^{+15.4}_{-10.1}$	$9.0^{+4.9}_{-4.9}$
CoKuTau4	$44.8^{+10.8}_{-12.1}$	$3.7^{+3.5}_{-1.4}$	$3.9^{+3.9}_{-2.8}$	$2.6^{+4.5}_{-2.3}$	$6.0^{+6.9}_{-0.6}$	$3.6^{+4.2}_{-7.1}$
. . .	$5.8^{+4.0}_{-2.6}$	$0.0^{+0.7}_{-0.4}$	$0.1^{+0.7}_{-0.2}$	$9.5^{+6.4}_{-4.3}$	$53.9^{+26.6}_{-17.1}$	$3.5^{+5.3}_{-3.2}$
DDTau	$50.2^{+19.1}_{-24.5}$	$5.2^{+5.6}_{-3.0}$	$2.1^{+5.1}_{-1.6}$	$1.1^{+4.2}_{-0.6}$	$1.7^{+11.5}_{-0.3}$	$22.9^{+9.0}_{-9.0}$
. . .	$16.1^{+9.4}_{-7.1}$	$0.1^{+1.1}_{-0.2}$	$0.0^{+2.2}_{-1.2}$	$0.2^{+3.9}_{-0.9}$	$14.5^{+4.7}_{-5.6}$	$0.0^{+1.1}_{-0.0}$
DETau	$37.3^{+6.9}_{-19.5}$	$7.2^{+3.8}_{-2.2}$	$1.1^{+3.2}_{-1.1}$	$0.0^{+1.4}_{-1.1}$	$31.3^{+6.3}_{-6.1}$	$8.5^{+5.4}_{-3.3}$
. . .	$15.1^{+11.0}_{-4.2}$	$0.0^{+5.3}_{-0.0}$	$0.0^{+2.5}_{-0.0}$	$9.3^{+15.2}_{-0.0}$	$18.9^{+14.7}_{-5.2}$	$0.0^{+4.6}_{-0.0}$

ID	Oli/Pyr[a] % (1.5 μm)	Ens % (1.5 μm)	For % (1.5 μm)	Sil % (1.5 μm)	Oli/Pyr[a] % (6.0 μm)	Sil % (6.0 μm)
DFTau	$19.2^{+3.8}_{-7.8}$	$3.7^{+3.9}_{-0.0}$	$0.0^{+4.9}_{-0.0}$	$2.8^{+6.5}_{-0.0}$	$71.3^{+18.8}_{-17.4}$	$0.0^{+7.3}_{-0.0}$
DHTau	$29.6^{+9.8}_{-10.3}$	$11.9^{+5.6}_{-3.1}$	$0.0^{+2.2}_{-0.4}$	$1.1^{+2.2}_{-1.0}$	$44.6^{+17.1}_{-22.4}$	$0.0^{+9.9}_{-0.0}$
$\cdots$	$17.3^{+20.6}_{-11.8}$	$5.7^{+17.2}_{-5.9}$	$4.3^{+8.0}_{-3.2}$	$0.0^{+22.9}_{-7.3}$	$22.4^{+9.4}_{-8.0}$	$12.4^{+10.2}_{-7.4}$
DKTau	$54.6^{+10.1}_{-12.9}$	$3.1^{+2.7}_{-1.9}$	$0.0^{+1.2}_{-0.0}$	$1.8^{+1.8}_{-0.0}$	$17.2^{+3.1}_{-3.7}$	$4.2^{+1.4}_{-1.1}$
DLTau	$38.0^{+17.1}_{-25.0}$	$10.1^{+10.2}_{-5.6}$	$0.0^{+6.0}_{-0.0}$	$8.8^{+7.6}_{-4.7}$	$24.4^{+12.3}_{-8.5}$	$10.7^{+7.4}_{-4.7}$
DMTau	$18.0^{+8.5}_{-13.8}$	$16.6^{+6.6}_{-7.4}$	$2.8^{+5.4}_{-1.4}$	$0.0^{+2.1}_{-0.0}$	$36.8^{+14.4}_{-10.8}$	$17.0^{+8.3}_{-12.1}$
$\cdots$	$2.0^{+2.6}_{-1.0}$	$0.8^{+2.8}_{-0.0}$	$2.1^{+5.9}_{-0.0}$	$8.8^{+9.7}_{-4.7}$	$29.7^{+21.5}_{-10.3}$	$6.8^{+4.2}_{-5.0}$
DNTau	$27.6^{+11.4}_{-3.5}$	$3.1^{+2.7}_{-2.0}$	$1.4^{+1.9}_{-0.9}$	$0.0^{+2.1}_{-0.0}$	$43.8^{+23.9}_{-26.5}$	$17.0^{+13.5}_{-4.4}$
$\cdots$	$46.4^{+53.9}_{-0.0}$	$0.0^{+38.7}_{-0.0}$	$3.6^{+16.8}_{-0.0}$	$0.0^{+>1.0}_{-0.0}$	$3.2^{+11.2}_{-0.0}$	$12.9^{+32.7}_{-0.0}$
DOTau	$52.2^{+28.2}_{-9.1}$	$4.5^{+5.7}_{-0.0}$	$5.3^{+6.3}_{-0.0}$	$1.9^{+6.2}_{-0.0}$	$19.9^{+14.9}_{-7.5}$	$13.1^{+5.0}_{-4.6}$
DPTau	$50.7^{+27.5}_{-15.8}$	$0.3^{+2.8}_{-0.0}$	$1.5^{+4.0}_{-0.0}$	$0.0^{+1.8}_{-0.0}$	$0.2^{+1.6}_{-0.0}$	$11.0^{+5.6}_{-0.0}$
$\cdots$	$44.4^{+18.0}_{-23.3}$	$0.0^{+5.4}_{-0.0}$	$7.8^{+5.1}_{-3.8}$	$0.0^{+2.7}_{-0.3}$	$4.0^{+1.2}_{-1.0}$	$3.1^{+2.3}_{-0.0}$
DQTau	$20.6^{+6.8}_{-8.1}$	$6.0^{+3.1}_{-2.0}$	$0.0^{+1.4}_{-0.0}$	$1.7^{+2.8}_{-1.0}$	$62.3^{+22.9}_{-34.4}$	$0.0^{+5.8}_{-0.0}$
$\cdots$	$30.8^{+36.9}_{-14.5}$	$0.0^{+12.6}_{-0.0}$	$4.6^{+8.4}_{-3.1}$	$0.0^{+11.7}_{-0.2}$	$21.1^{+36.2}_{-10.5}$	$29.1^{+21.2}_{-11.9}$
DRTau	$31.6^{+9.3}_{-8.7}$	$0.6^{+1.5}_{-0.0}$	$1.6^{+2.1}_{-1.1}$	$0.0^{+1.0}_{-0.0}$	$20.4^{+9.9}_{-9.6}$	$19.8^{+6.4}_{-4.7}$
DSTau	$17.4^{+13.7}_{-4.1}$	$6.2^{+3.4}_{-3.1}$	$0.2^{+1.4}_{-0.0}$	$0.0^{+1.1}_{-0.0}$	$36.4^{+11.9}_{-10.5}$	$0.0^{+4.5}_{-0.0}$
$\cdots$	$13.4^{+10.9}_{-6.7}$	$20.1^{+17.0}_{-10.8}$	$0.1^{+3.6}_{-1.4}$	$7.0^{+7.3}_{-4.8}$	$11.0^{+7.6}_{-4.9}$	$6.3^{+6.0}_{-4.1}$
F04147+2822	$71.2^{+11.8}_{-25.9}$	$0.0^{+4.4}_{-0.0}$	$0.0^{+4.0}_{-0.0}$	$0.1^{+2.8}_{-0.0}$	$3.6^{+3.4}_{-0.1}$	$12.0^{+5.3}_{-3.4}$
F04192+2647	$49.0^{+10.0}_{-11.6}$	$8.7^{+3.6}_{-4.0}$	$0.9^{+3.3}_{-0.5}$	$0.7^{+4.2}_{-0.1}$	$21.5^{+11.8}_{-9.9}$	$12.1^{+4.2}_{-4.0}$
$\cdots$	$16.1^{+12.1}_{-6.0}$	$5.3^{+9.9}_{-3.2}$	$11.7^{+16.0}_{-7.1}$	$0.0^{+5.8}_{-0.0}$	$19.4^{+12.2}_{-7.1}$	$9.7^{+8.5}_{-4.8}$
F04262+2654	$53.7^{+59.3}_{-16.5}$	$14.9^{+14.3}_{-5.7}$	$0.0^{+8.6}_{-0.0}$	$3.7^{+9.6}_{-3.1}$	$19.1^{+12.1}_{-8.9}$	$2.6^{+7.6}_{-2.2}$
F04297+2246	$34.0^{+7.8}_{-16.4}$	$9.5^{+4.4}_{-2.9}$	$2.8^{+4.4}_{-1.9}$	$0.0^{+3.2}_{-0.0}$	$44.1^{+9.8}_{-26.1}$	$0.9^{+12.5}_{-1.0}$
$\cdots$	$22.8^{+66.2}_{-0.0}$	$0.0^{+26.4}_{-0.0}$	$18.7^{+18.5}_{-15.3}$	$5.4^{+35.6}_{-0.0}$	$21.3^{+29.8}_{-5.7}$	$3.5^{+23.3}_{-0.0}$
F04297+2246A	$45.9^{+9.6}_{-10.3}$	$9.0^{+2.9}_{-3.1}$	$3.4^{+3.0}_{-2.4}$	$2.9^{+2.3}_{-1.5}$	$23.9^{+4.1}_{-5.3}$	$2.1^{+8.0}_{-0.0}$
$\cdots$	$20.1^{+11.1}_{-9.1}$	$0.2^{+2.4}_{-0.0}$	$4.3^{+5.4}_{-0.0}$	$0.0^{+1.4}_{-0.0}$	$11.2^{+6.3}_{-5.2}$	$29.2^{+15.0}_{-15.7}$
F04570+2520	$64.1^{+24.3}_{-22.8}$	$5.8^{+6.2}_{-5.2}$	$6.6^{+6.4}_{-0.0}$	$0.0^{+4.7}_{-0.0}$	$20.5^{+11.0}_{-4.3}$	$0.0^{+3.2}_{-0.3}$
$\cdots$	$0.0^{+3.6}_{-0.9}$	$0.0^{+7.3}_{-0.0}$	$13.7^{+9.1}_{-13.9}$	$15.7^{+7.4}_{-12.3}$	$21.5^{+9.9}_{-17.6}$	$9.0^{+2.6}_{-7.4}$
FMTau	$12.4^{+2.5}_{-9.9}$	$8.2^{+3.2}_{-3.6}$	$3.3^{+6.0}_{-1.4}$	$0.0^{+1.5}_{-0.0}$	$13.0^{+5.8}_{-5.4}$	$5.0^{+7.4}_{-0.7}$
$\cdots$	$6.4^{+10.5}_{-0.0}$	$1.1^{+3.7}_{-0.0}$	$1.3^{+17.3}_{-0.0}$	$5.4^{+14.0}_{-0.0}$	$28.3^{+17.3}_{-9.4}$	$25.4^{+45.6}_{-7.9}$
FNTau	$47.1^{+7.4}_{-14.4}$	$10.9^{+5.0}_{-3.7}$	$0.1^{+3.9}_{-0.0}$	$3.2^{+3.2}_{-2.3}$	$20.1^{+2.7}_{-7.2}$	$0.0^{+14.5}_{-0.0}$
$\cdots$	$19.0^{+68.3}_{-0.0}$	$1.3^{+16.2}_{-0.0}$	$2.9^{+14.3}_{-0.0}$	$1.8^{+36.4}_{-0.0}$	$18.8^{+56.1}_{-0.0}$	$23.6^{+102.6}_{-0.0}$
FOTau	$20.6^{+10.7}_{-12.0}$	$6.6^{+10.5}_{-2.3}$	$0.0^{+5.4}_{-0.0}$	$5.6^{+13.5}_{-0.0}$	$52.1^{+23.4}_{-18.6}$	$0.0^{+19.4}_{-0.0}$
FPTau	$5.5^{+11.8}_{-3.6}$	$0.0^{+3.2}_{-0.2}$	$0.0^{+1.7}_{-0.0}$	$0.0^{+1.1}_{-0.0}$	$64.1^{+25.1}_{-20.7}$	$0.0^{+11.6}_{-1.1}$
$\cdots$	$6.3^{+5.5}_{-3.5}$	$15.5^{+11.9}_{-10.1}$	$2.8^{+1.8}_{-0.0}$	$8.5^{+9.4}_{-0.0}$	$33.5^{+18.2}_{-9.2}$	$5.0^{+4.6}_{-0.0}$
FQTau	$49.6^{+32.6}_{-28.2}$	$9.1^{+13.6}_{-4.1}$	$3.0^{+8.0}_{-2.4}$	$4.8^{+7.8}_{-3.0}$	$9.0^{+7.0}_{-3.6}$	$0.0^{+2.7}_{-0.0}$
FSTau	$42.6^{+11.4}_{-14.7}$	$0.0^{+2.1}_{-0.0}$	$0.0^{+2.2}_{-0.0}$	$0.0^{+2.5}_{-0.0}$	$17.0^{+5.8}_{-6.1}$	$4.6^{+5.2}_{-3.2}$
FTTau	$13.9^{+8.6}_{-3.6}$	$3.9^{+3.4}_{-1.6}$	$2.1^{+2.1}_{-1.4}$	$0.1^{+1.6}_{-0.0}$	$49.7^{+15.9}_{-27.4}$	$6.4^{+10.3}_{-3.6}$
$\cdots$	$48.8^{+22.9}_{-5.6}$	$0.0^{+23.7}_{-0.0}$	$2.9^{+11.9}_{-0.0}$	$0.5^{+35.3}_{-0.0}$	$12.0^{+30.6}_{-0.0}$	$18.6^{+15.1}_{-0.0}$
FVTau	$22.7^{+19.4}_{-0.0}$	$12.8^{+8.7}_{-7.2}$	$9.0^{+11.8}_{-0.0}$	$0.0^{+3.0}_{-0.0}$	$43.2^{+12.9}_{-13.5}$	$6.9^{+16.1}_{-0.0}$
FXTau	$46.5^{+10.5}_{-13.3}$	$6.3^{+4.2}_{-2.5}$	$0.0^{+2.1}_{-0.0}$	$0.0^{+1.6}_{-0.0}$	$4.0^{+3.6}_{-0.0}$	$8.0^{+2.6}_{-1.8}$
$\cdots$	$25.3^{+16.6}_{-8.6}$	$0.2^{+2.7}_{-0.0}$	$0.2^{+4.2}_{-0.0}$	$1.7^{+10.7}_{-0.0}$	$33.3^{+16.6}_{-14.1}$	$9.6^{+21.9}_{-0.0}$
FZTau	$19.1^{+10.8}_{-5.4}$	$4.4^{+2.3}_{-1.9}$	$1.5^{+2.2}_{-0.5}$	$0.0^{+2.8}_{-0.0}$	$25.0^{+6.4}_{-8.4}$	$11.1^{+4.0}_{-4.2}$

ID	Oli/Pyr[a] % (1.5 μm)	Ens % (1.5 μm)	For % (1.5 μm)	Sil % (1.5 μm)	Oli/Pyr[a] % (6.0 μm)	Sil % (6.0 μm)
GGTau	$54.2^{+15.5}_{-15.3}$	$0.0^{+2.1}_{-0.0}$	$1.9^{+2.8}_{-1.3}$	$0.0^{+1.1}_{-0.0}$	$16.5^{+4.7}_{-3.8}$	$15.7^{+4.9}_{-4.4}$
GHTau	$27.3^{+15.0}_{-11.6}$	$7.3^{+3.2}_{-4.0}$	$0.8^{+2.7}_{-0.8}$	$4.1^{+3.1}_{-2.9}$	$45.4^{+26.6}_{-14.6}$	$0.0^{+4.3}_{-0.0}$
$\cdots$	$11.5^{+8.2}_{-6.5}$	$4.4^{+1.8}_{-3.2}$	$1.0^{+1.8}_{-1.0}$	$12.6^{+10.3}_{-8.0}$	$32.4^{+19.8}_{-14.5}$	$19.7^{+18.4}_{-13.8}$
GITau	$39.3^{+14.0}_{-7.7}$	$5.7^{+2.6}_{-2.7}$	$1.6^{+2.0}_{-0.0}$	$1.0^{+1.8}_{-0.0}$	$6.4^{+1.8}_{-1.8}$	$8.4^{+2.9}_{-2.1}$
$\cdots$	$20.5^{+10.5}_{-7.6}$	$0.0^{+2.1}_{-0.0}$	$0.0^{+2.7}_{-0.0}$	$0.1^{+2.8}_{-0.0}$	$33.9^{+14.4}_{-12.7}$	$8.1^{+9.2}_{-4.9}$
GKTau	$18.0^{+3.5}_{-6.6}$	$3.7^{+0.8}_{-1.4}$	$0.0^{+0.7}_{-0.0}$	$1.7^{+0.9}_{-0.7}$	$7.3^{+1.8}_{-1.8}$	$1.8^{+0.8}_{-0.8}$
GMAur	$16.0^{+5.5}_{-4.1}$	$12.2^{+3.4}_{-4.2}$	$14.9^{+5.6}_{-0.0}$	$0.0^{+1.2}_{-0.0}$	$1.2^{+10.8}_{-0.0}$	$15.4^{+4.5}_{-6.7}$
$\cdots$	$9.6^{+14.1}_{-0.0}$	$3.8^{+20.4}_{-0.0}$	$0.0^{+8.6}_{-0.0}$	$17.4^{+17.6}_{-0.0}$	$33.6^{+32.2}_{-0.0}$	$1.3^{+14.1}_{-0.0}$
GOTau	$63.2^{+24.7}_{-37.8}$	$3.3^{+6.0}_{-5.3}$	$0.0^{+5.4}_{-0.0}$	$5.6^{+7.8}_{-4.8}$	$12.4^{+6.4}_{-5.3}$	$0.0^{+2.0}_{-0.0}$
HKTau	$37.5^{+6.1}_{-21.5}$	$7.7^{+2.8}_{-4.7}$	$8.2^{+4.0}_{-0.0}$	$0.0^{+3.3}_{-0.0}$	$18.6^{+8.1}_{-6.0}$	$24.8^{+4.5}_{-11.5}$
$\cdots$	$13.5^{+33.1}_{-3.4}$	$6.7^{+33.1}_{-0.0}$	$2.9^{+5.6}_{-0.0}$	$7.4^{+64.7}_{-0.0}$	$21.5^{+25.3}_{-6.3}$	$10.6^{+14.0}_{-6.4}$
HNTau	$45.5^{+12.1}_{-7.7}$	$0.0^{+1.3}_{-0.0}$	$0.0^{+1.3}_{-0.0}$	$0.0^{+1.3}_{-0.0}$	$22.9^{+4.8}_{-4.6}$	$16.8^{+4.5}_{-3.2}$
HOTau	$34.6^{+12.9}_{-8.6}$	$6.2^{+3.6}_{-3.9}$	$2.2^{+5.5}_{-0.0}$	$0.4^{+2.2}_{-0.0}$	$43.0^{+11.7}_{-17.1}$	$0.0^{+10.3}_{-0.0}$
$\cdots$	$37.6^{+23.2}_{-11.3}$	$0.4^{+5.9}_{-0.0}$	$0.3^{+2.0}_{-0.0}$	$4.2^{+7.1}_{-3.4}$	$8.3^{+7.0}_{-3.6}$	$9.3^{+3.2}_{-5.8}$
HPTau	$22.1^{+3.6}_{-4.9}$	$1.1^{+1.9}_{-0.0}$	$0.0^{+1.3}_{-0.0}$	$0.9^{+1.3}_{-0.0}$	$14.3^{+4.4}_{-2.3}$	$3.4^{+1.3}_{-1.3}$
Haro6-37	$45.0^{+16.2}_{-27.5}$	$10.4^{+5.8}_{-5.4}$	$2.6^{+4.5}_{-0.0}$	$7.0^{+6.5}_{-4.0}$	$17.2^{+12.2}_{-7.0}$	$0.0^{+7.1}_{-0.0}$
IPTau	$33.0^{+9.9}_{-7.5}$	$4.5^{+4.4}_{-2.4}$	$3.9^{+5.0}_{-2.5}$	$0.0^{+1.2}_{-0.0}$	$18.7^{+12.5}_{-8.3}$	$8.5^{+3.2}_{-4.1}$
$\cdots$	$19.3^{+18.2}_{-8.9}$	$4.2^{+18.2}_{-0.0}$	$1.8^{+9.0}_{-0.0}$	$13.7^{+8.5}_{-5.7}$	$32.3^{+11.1}_{-6.9}$	$1.7^{+12.0}_{-1.4}$
IQTau	$30.7^{+8.8}_{-8.7}$	$8.4^{+3.6}_{-2.4}$	$2.7^{+3.5}_{-1.4}$	$1.6^{+2.4}_{-0.9}$	$28.7^{+6.8}_{-11.3}$	$8.7^{+3.9}_{-3.8}$
$\cdots$	$43.9^{+14.6}_{-12.9}$	$0.0^{+4.6}_{-0.0}$	$0.6^{+3.1}_{-0.0}$	$0.0^{+6.5}_{-0.0}$	$14.7^{+9.1}_{-3.3}$	$14.1^{+12.4}_{-7.1}$
ISTau	$47.8^{+13.5}_{-16.1}$	$19.0^{+7.3}_{-5.2}$	$5.1^{+7.1}_{-4.2}$	$0.3^{+4.4}_{-0.0}$	$9.4^{+8.4}_{-3.0}$	$0.0^{+7.7}_{-0.0}$
$\cdots$	$26.5^{+42.8}_{-13.3}$	$0.0^{+76.9}_{-0.0}$	$14.0^{+97.4}_{-0.0}$	$4.7^{+66.6}_{-0.0}$	$26.9^{+67.9}_{-6.9}$	$7.6^{+47.0}_{-0.0}$
LkCa15	$21.6^{+11.5}_{-6.1}$	$7.7^{+2.7}_{-2.7}$	$6.3^{+3.5}_{-3.0}$	$0.0^{+0.6}_{-0.0}$	$4.8^{+2.7}_{-0.0}$	$0.8^{+3.1}_{-0.0}$
$\cdots$	$16.0^{+7.7}_{-6.8}$	$6.1^{+5.6}_{-3.6}$	$0.0^{+1.5}_{-0.0}$	$6.6^{+6.3}_{-4.9}$	$16.2^{+8.1}_{-6.9}$	$13.7^{+9.5}_{-7.0}$
RWAur	$39.0^{+9.1}_{-23.1}$	$2.3^{+3.9}_{-0.0}$	$0.0^{+1.8}_{-0.0}$	$0.0^{+1.5}_{-0.0}$	$12.4^{+3.3}_{-8.7}$	$18.3^{+6.7}_{-6.8}$
RYTau	$69.7^{+13.3}_{-10.2}$	$1.9^{+3.3}_{-0.0}$	$0.0^{+1.6}_{-0.0}$	$1.0^{+2.1}_{-0.0}$	$3.3^{+1.8}_{-1.1}$	$0.0^{+0.2}_{-0.0}$
SUAur	$49.7^{+8.5}_{-8.5}$	$1.2^{+1.8}_{-0.0}$	$2.4^{+3.3}_{-0.0}$	$0.0^{+0.6}_{-0.0}$	$3.9^{+1.9}_{-1.7}$	$21.3^{+3.1}_{-3.6}$
UYAur	$54.3^{+11.1}_{-13.1}$	$0.0^{+1.9}_{-0.0}$	$1.3^{+3.6}_{-0.0}$	$0.0^{+1.3}_{-0.0}$	$14.1^{+3.9}_{-6.2}$	$10.4^{+7.2}_{-0.0}$
V710Tau	$39.1^{+17.8}_{-28.1}$	$8.5^{+6.9}_{-5.0}$	$6.0^{+5.9}_{-3.5}$	$8.0^{+6.2}_{-4.6}$	$3.7^{+1.9}_{-1.8}$	$3.3^{+2.5}_{-1.3}$
V773Tau	$40.9^{+12.7}_{-17.2}$	$4.3^{+9.4}_{-0.0}$	$0.0^{+1.8}_{-0.0}$	$0.0^{+8.0}_{-0.0}$	$10.9^{+5.7}_{-3.8}$	$12.5^{+5.6}_{-6.3}$
V836Tau	$32.4^{+16.9}_{-14.5}$	$9.1^{+4.2}_{-3.3}$	$2.8^{+3.4}_{-1.9}$	$3.9^{+2.1}_{-2.8}$	$45.1^{+9.7}_{-35.6}$	$0.0^{+8.7}_{-0.0}$
$\cdots$	$32.6^{+52.5}_{-19.6}$	$3.9^{+23.7}_{-0.0}$	$1.7^{+12.2}_{-0.0}$	$0.5^{+24.0}_{-0.0}$	$17.0^{+30.6}_{-3.8}$	$1.5^{+3.7}_{-1.5}$
V955Tau	$59.3^{+15.0}_{-32.6}$	$4.6^{+5.8}_{-2.1}$	$0.0^{+3.0}_{-0.0}$	$0.0^{+2.9}_{-0.1}$	$11.9^{+4.7}_{-3.6}$	$7.2^{+6.7}_{-1.8}$
VYTau	$18.1^{+4.7}_{-8.2}$	$1.1^{+7.2}_{-0.1}$	$0.0^{+14.7}_{-0.0}$	$0.6^{+7.6}_{-0.0}$	$74.0^{+14.1}_{-47.6}$	$0.3^{+18.0}_{-0.0}$
ZZTauIRS	$76.1^{+12.9}_{-21.8}$	$0.3^{+4.3}_{-0.5}$	$3.3^{+4.8}_{-1.9}$	$0.0^{+2.9}_{-0.0}$	$0.0^{+1.6}_{-0.0}$	$2.8^{+7.3}_{-0.0}$
$\cdots$	$39.4^{+18.7}_{-15.4}$	$0.0^{+3.7}_{-0.4}$	$9.1^{+7.5}_{-5.2}$	$9.7^{+9.3}_{-6.1}$	$7.0^{+5.2}_{-3.5}$	$4.6^{+4.3}_{-2.9}$
Upper Scorpius						
PBB2002 J160357.9	$42.9^{+14.8}_{-24.5}$	$0.0^{+0.5}_{-4.5}$	$0.0^{+4.7}_{-0.0}$	$0.0^{+3.9}_{-0.0}$	$46.8^{+28.8}_{-32.4}$	$0.0^{+10.9}_{-0.0}$
PBB2002 J160823.2	$27.1^{+2.5}_{-24.1}$	$5.9^{+3.9}_{-3.6}$	$0.0^{+7.7}_{-0.0}$	$0.6^{+10.4}_{-0.0}$	$60.1^{+38.8}_{-22.7}$	$0.0^{+5.1}_{-0.1}$
PBB2002 J160900.7	$42.3^{+14.3}_{-17.3}$	$4.1^{+3.7}_{-2.4}$	$0.0^{+2.5}_{-0.0}$	$0.0^{+1.0}_{-0.0}$	$24.9^{+2.9}_{-16.8}$	$8.0^{+4.9}_{-4.0}$
PBB2002 J160959.4	$61.9^{+16.5}_{-50.2}$	$10.6^{+12.0}_{-8.1}$	$0.0^{+7.6}_{-0.0}$	$0.0^{+4.5}_{-0.0}$	$3.1^{+5.9}_{-0.9}$	$1.2^{+11.7}_{-0.2}$
PBB2002 J161115.3	$58.7^{+11.1}_{-26.8}$	$3.1^{+5.0}_{-2.0}$	$0.0^{+6.7}_{-0.0}$	$1.5^{+2.6}_{-0.4}$	$9.2^{+3.2}_{-4.6}$	$5.3^{+1.3}_{-4.9}$

ID	Oli/Pyr[a] % (1.5 μm)	Ens % (1.5 μm)	For % (1.5 μm)	Sil % (1.5 μm)	Oli/Pyr[a] % (6.0 μm)	Sil % (6.0 μm)
PBB2002 J161420.2	$67.7^{+7.9}_{-7.8}$	$0.6^{+0.9}_{-0.0}$	$0.8^{+1.2}_{-0.0}$	$0.0^{+0.4}_{-0.0}$	$15.2^{+2.8}_{-1.5}$	$7.9^{+1.3}_{-1.3}$
PZ99 J160357.6	$6.1^{+9.2}_{-0.0}$	$3.8^{+2.9}_{-0.0}$	$0.2^{+2.2}_{-0.0}$	$0.0^{+2.6}_{-0.0}$	$87.1^{+19.9}_{-46.7}$	$0.0^{+5.1}_{-0.0}$
PZ99 J161411.0	$8.8^{+4.7}_{-0.0}$	$3.9^{+3.5}_{-0.0}$	$0.0^{+1.4}_{-0.0}$	$0.0^{+4.1}_{-0.0}$	$84.8^{+8.6}_{-55.2}$	$0.0^{+3.0}_{-0.0}$
ScoPMS31	$72.4^{+39.8}_{-61.0}$	$4.6^{+10.7}_{-3.7}$	$0.0^{+9.0}_{-1.9}$	$1.9^{+9.2}_{-1.4}$	$6.6^{+4.2}_{-6.2}$	$0.0^{+1.5}_{-0.0}$
η Chamaeleontis						
J0843	$44.6^{+19.9}_{-21.9}$	$5.9^{+7.6}_{-0.0}$	$0.0^{+10.2}_{-0.0}$	$1.6^{+11.6}_{-0.0}$	$13.6^{+19.2}_{-0.0}$	$0.0^{+3.9}_{-0.0}$
RECX-5	$12.3^{+15.6}_{-3.5}$	$23.9^{+13.9}_{-0.0}$	$0.0^{+8.0}_{-0.0}$	$8.0^{+6.9}_{-3.3}$	$7.1^{+18.9}_{-0.0}$	$0.0^{+10.0}_{-0.0}$
RECX-9	$31.6^{+15.8}_{-24.2}$	$0.9^{+7.0}_{-0.0}$	$5.4^{+5.8}_{-3.2}$	$4.6^{+10.8}_{-2.1}$	$3.3^{+3.0}_{-1.1}$	$0.8^{+8.3}_{-0.0}$
RECX-11	$26.8^{+15.7}_{-14.4}$	$8.0^{+10.5}_{-0.0}$	$0.0^{+2.7}_{-0.0}$	$3.4^{+3.7}_{-1.9}$	$17.6^{+8.1}_{-6.6}$	$0.0^{+1.9}_{-0.0}$

Table A.2 – Intermediate and large dust composition derived using the "B2C" procedure.[b]

[a] Amorphous olivine and pyroxene combined.

[b] For each object, the first line corresponds to the warm component abundances, while the second line corresponds to the cold component abundances, when available.